ECE Technical Reports

Electrical and Computer Engineering

9-1-1993

Invariant Reconstruct ion of Curves and Surfaces using a First Order Regularization

June Ho Yi
Purdue University School of Electrical Engineering

David M. Chelberg
Purdue University School of Electrical Engineering

Invariant Reconstruction of Curves and Surfaces using a First Order Regularization

June Ho Yi
David M. Chelberg

TR-EE 93-30
September 1993

School of Electrical Engineering
Purdue University
West Lafayette, Indiana 47907-1285

Invariant Reconstruction of Curves and Surfaces using a First Order Regularization[1]

June Ho Yi
David M Chelberg

Geometric Modeling and Perceptual Processing Laboratory
School of Electrical Engineering
Purdue University
West Lafayette, Indiana 47907-1285

'This work was supported by a Digital Equipment Corporation Faculty Incentives for Excellence Grant, and by NSF Grant number IRI-9011421.

Contents

List of Figures

List of Tables

Abstract

This paper describes the application of a first order regularization technique to the problem of reconstruction of curves and surfaces from sparse data. The reconstruction methods achieve approximate invariance, sharp preservation of discontinuities and are robust to the smoothing parameter λ. The robustness property to λ allows a free choice of the smoothing parameter λ without struggling to determine an optimal λ that provides the best reconstruction. A new approximately invariant first order stabilizing function for surface reconstruction is obtained by employing a first order Taylor expansion of a nonconvex invariant stabilizing function that is expanded at the estimated value of the squared gradient instead of at zero. The data compatibility measure used is the squared perpendicular distance between the reconstructed surface and the constraint surface. This combination of stabilizing function and data compatibility measure is necessary to achieve invariance with respect to rotations and translations of the surfaces being reconstructed. Sharp preservation of discontinuities is achieved by a weighted sum of adjacent pixels such that the adjacent pixels that are more likely to be in different regions are less weighted. The ideas employed for surface reconstruction are also applied to curve reconstruction. The results indicate that the proposed methods for curve and surface reconstruction perform well on sparse noisy range data. Curved surfaces (or curved sections in the case of curve reconstruction) are well reconstructed even though a first order model is employed. In addition, the volume between two surfaces normalized by the surface area is proposed as an invariant measure for the comparison of reconstruction results. Similarly, the area between two curves normalized by the arc length is proposed for comparing curve reconstruction results.

Chapter 1

Introduction

Considerable research has been devoted to the problem of the reconstruction of curves [24] [25] [19] [4] [16] and surfaces [30] [31] [32] [2] [3] [4] [34] [6] [27] [26] [9] [14] [29] [28] [20] [17] [1] [23] [22] [8] [18] [5] [11] [19] [10]. Reconstruction is necessary to derive a complete representation of a curve or surface from sparse noisy sets of geometric information, such as depth and orientation or other sources of information. A reconstructed curve or surface is an intermediate representation to bridge the gap between sensor data and a symbolic description of a curve or surface. An ideal algorithm for reconstruction should have several properties. First, reconstruction must be invariant with respect to viewpoint, that is, to rotations and translations of the curves and surfaces being reconstructed. This is especially important when reconstruction is part of an object recognition system. In this case a change in this intermediate representation may cause a change in any symbolic description that is derived, resulting in failure to identify the objects in a scene. Second, it is desirable to firtd discontinuities both in depth and orientation. A reconstruction algorithm, if detection of discontinuities is not simultaneously carried out in the reconstruction process, should at least sharply preserve regions near discontinuities for a later stage of discontinuity detection.

The general term regularization is used for any method to make an ill-posed problem well-posed. The main idea for restoring well-posedness from ill-posedness is to restrict the class of admissible solutions by introducing suitable a *priori* knowledge. Much research on the problem of surface reconstruction is found in the context of deterministic regularization [34] [6] [26] [27] [1] [22] [23] [30] [31] [32] [3] [4] [5] [11] [19] and stochastic regularization [9] [14] [29] [28] [7] [18] [10]. Deterministic regularization uses smoothness constraints on the possible solutions as a *priori* knowledge whereas, in stochastic regularization, a *priori* knowledge is represented in terms of probability distributions. A *priori* knowledge in stochastic regularization can be formulated in terms of a Markov random field (MRF) model of the surface within the Bayesian framework. In most cases, the result is a nonconvex problem. The solution to these nonconvex problems has been obtained by using simulated annealing [15], Gibbs sampler [10], or by deterministic approximation to a statistical model such as the Mean Field approximation [9]. However, the methods suggested for finding a solution are either not guaranteed to converge to a global minimum or are computationally very expensive. From now on, the term regularization will refer to deterministic regularization.

Invariant reconstruction of surfaces in the context of regularization has been investigated by approximating an invariant energy function. Second order models that are capable of invariant reconstruction are investigated in [3] [2] [27]. Blake and Zisserman [3] [2] used a convex approximation to the explicit expression of a second order invariant form and Stevenson and Delp [27] made a convex approximation to the parametric form. However, a convex approximation to the first order invariant form has not been previously reported. In addition, these other approaches do not explicitly consider sharp preservation of discontinuities. Many researchers have attempted to reconstruct surfaces with sharp preservation of discontinuities [26] [23] [22] [6] [34] [20] [19] [32] [31]. Most efforts toward discontinuity-preserving reconstruction share a common property. Preservation of discontinuities is achieved by properly chosen weighting functions by which the adjacent pixels or the basis functions for spline that are more likely to belong to different regions are less or not weighted in the computation of a reconstructed pixel value. Discontinuities are detected during the reconstruction process by adding to an energy (cost) function a term that depends on the number or extent of the discontinuities [19] [3] [2] [4]. However, this makes the problem nonconvex and finding the solution is computationally expensive and not guaranteed to find a global minimum. Some researchers have detected discontinuities as a preprocessing step for surface reconstruction [17] [32] [6]. However, none of these methods considers invariance of the reconstruction result at the same time. A detailed description of the past work on discontinuity-preserving reconstruction is found in chapter 4. Many ideas used for curve reconstruction are one dimensional analogs of those for surface reconstruction. For invariant reconstruction of curves, Stevenson and Delp [25]'s work is a one dimensional analog of [27]. For discontinuity-preserving reconstruction of curves, they conceived discontinuities as a deviation from the smoothness assumption and used the theory of robust statistics as in their corresponding surface reconstruction work [26]. Lee and Pavlidis [16] also used a cubic spline but they explicitly detected discontinuities.

In this paper, we apply regularization techniques using first order convex energy functionals to the problems of curve reconstruction and surface reconstruction. We propose a novel form of energy functional for curve reconstruction and surface reconstruction that achieves approximate invariance, sharp preservation of discontinuities, and robustness of reconstruction performance with respect to the smoothing parameter λ. That is, reconstruction results are almost the same for various smoothing parameter X's in a wide range. This property is significant in that we can freely choose the smoothing parameter X without struggling to determine which X provides the best reconstruction result. In the past, some researchers have proposed methods to compute an optimal smoothing parameter X according to a chosen criterion. However, most researchers have selected their smoothing parameter X's in an ad hoc way because of the difficulty in finding an optimal λ. In order to compute an optimal λ, it is necessary to accurately characterize and estimate the noise in the data. This difficulty makes the problem of finding an optimal X difficult to solve. Various ways of choosing an optimal X in the case of quadratic regularization criteria are discussed in [33]. The effort to compute an optimal X can be saved if the reconstruction method is robust. A first order model was employed instead of a second order model because a first order model entails significantly less computational effort than a second order model. Surface reconstruction results are compared using an invariant quantitative measure together with visual displays of the reconstruction results. The volume between two surfaces normalized by surface area is used as an invariant quantitative measure for comparing surface reconstruction results. This measure is invariant with respect to an arbitrary coordinate system, that is, it provides the same measures for reconstruction results of a surface in different coordinate systems. Similarly, we employ the area between two curves normalized by the arc length as an invariant measure for comparing curve reconstruction results. The ideas for curve reconstruction are not described separately. Curve reconstruction uses the same ideas as those applied to surface reconstruction, i.e., the ideas for curve reconstruction are one dimensional analogs of those for surface reconstruction. Stevenson and Delp's work, [25] and [24] are just one dimensional cases of [27] and [26] respectively. Blake and Zisserman's work on curve reconstruction is found with their surface reconstruction work.

The algorithm for surface reconstruction consists of three steps: an initial reconstruction, partial derivative estimates from the initial reconstruction result, and then a second reconstruction which uses the estimated derivatives. We estimate the partial derivatives of a surface to be reconstructed in advance. The estimated derivatives are inserted as constants into an approximately invariant energy functional (second reconstruction) which is then convex. The importance of the estimated derivatives is that they improve the performance of the second reconstruction with respect to invariance and discontinuity preservation. These derivatives need not be perfect to achieve a substantial improvement after the second reconstruction. In order to estimate the derivatives, we reconstruct the input surface using a regularization technique. However, any other appropriate method can be used to produce the derivative estimates. The entire algorithm proceeds by first reconstructing the input noisy range data (dense or sparse) using a simple membrane model. This energy model is not capable of producing invariant nor discontinuity-preserving reconstruction. It also does not have the robustness property to the smoothing parameter λ. Second, partial derivatives $\hat{z}_x$ and $\hat{z}_y$ are estimated from the reconstruction result just obtained where $\hat{z}_x$ and $\hat{z}_y$ denote the partial derivative estimate with respect to x and y direction, respectively. Third, the original noisy range input data (dense or sparse) is reconstructed using our proposed energy function that achieves both invariance and preservation of discontinuities, with the use of the partial derivative estimates computed in the second step.

A new first order stabilizing function is obtained by employing a first order Taylor expansion of a nonconvex invariant stabilizing function that is expanded at the estimated value of squared gradient instead of at zero. The new first order stabilizing function reduces the approximation error better than the commonly used membrane energy functional where surfaces of an image are steep. The squared perpendicular distance between the reconstructed surface and the constraint surface is used as an invariant data compatibility measure. It is based on the assumption that they are roughly parallel [2]. This assumption is related to the particular noise model employed. Here the assumption is that, in an image, more steeply inclined surfaces show greater noise than flatter surfaces. If noise is uniformly distributed in the direction of the normal to a surface, when the surface is imaged from a particular viewpoint, then more steeply inclined regions will have greater uncertainty in their measurements. This agrees with the research result by Ikeuchi and Kanade [13] where they reported a noise model of typical light-stripe range finder. According to their findings, the larger the angle between the surface normal and the illuminator direction of a light stripe, the larger uncertainty exists in the sensed z value. Combining the stabilizing function and the data compatibility measure, we obtain a novel form of energy function in which the gradient information is incorporated. For simplicity, we will use ***forward finite difference*** in order to approximate the continuous surface although it is possible to discretize it using a variety of finite elements. Sharp preservation of discontinuities is achieved by a weighted sum of adjacent pixels in that the adjacent pixels which are more likely to be in different regions are less weighted. The estimates, $\hat{z}_x$ and 2, obtained from a reconstruction result using the simple membrane model are provided for the second invariant and discontinuity-preserving reconstruction. Given a novel form of the energy function with gradient information incorporated, another problem is how to estimate the derivative, $\hat{z}_x$ and $\hat{z}_y$ at the location of node (i,j) because the reconstruction performance may degrade on the disagreement of the weighting pattern of the updating equation derived from the energy with the method of estimating the derivative. Two basic schemes that are commonly used are as follows. One is the forward difference which is a biased estimate of the derivative. Another estimate that is not biased is the central difference. We investigate two alternative reconstruction methods in order to see the effect of the method of estimating the derivative on the reconstruction results. One method is the use of the biased derivative estimate for the obtained novel form of energy. The other method is the use of the unbiased derivative estimate with an appropriate adjustment of the same energy for the purpose of preservation of discontinuities. Both methods achieve invariance and preservation of discontinuities. However, the latter method is recommended for surface reconstruction because reconstruction using this method is also robust to the smoothing parameter λ. One dimensional analogs of the ideas employed in surface reconstruction are derived for curve reconstruction in chapter 6.

In chapter 7, the performance of three reconstruction methods for both curve reconstruction and surface reconstruction are compared. Let us denote these three reconstruction methods as follows.

- FIT : ordinary reconstruction using the commonly used membrane energy model. Corresponding energy function is found in chapter 2.
- IDFIT-BIASED : invariant and discontinuity-preserving reconstruction using the energy (before adjustment) with the derivative estimated by the biased estimate method. Corresponding energy function and updating equations are found in section 4.1.
- IDFIT-UNBIASED : invariant and discontinuity-preserving reconstruction using the energy (after adjustment) with the derivative estimated by the unbiased estimate method. Corresponding energy function and updating equations are found in section 4.2.

It will be shown in chapter 7 that reconstruction results from best to worst are ordered as IDFIT-UNBIASED, IDFIT-BIASED, and FIT. For the invariance property, the performance of IDFIT-BIASED and IDFIT-UNBIASED do not show much difference while their performance is much better than that of FIT. IDFIT-UNBIASED performs very well on sparse noisy data for both curve reconstruction and surface reconstruction. In addition, curved surfaces (or curved sections in case of curve reconstruction) are well reconstructed although first order energy models are employed.

The contributions of this work are as follows: First, a new technique is presented for reconstruction of curves and surfaces using a first order energy function that achieves invariance, preservation of discontinuities, and robustness to the smoothing (or equivalently scale) parameter A. Second, an invariant measure for comparing reconstruction results is proposed, and a computationally efficient method for computing the measure is presented.

This paper is organized as follows. The development of the ideas behind the reconstruction algorithms will be presented for surface reconstruction alone. Chapter 6 will present the analogous ideas applied to the curve reconstruction problem. Due to the similarity of the two methods, chapter 6 relies upon the theoretical development presented for surface reconstruction. Chapters 2-5 will describe in detail the process of surface reconstruction. In chapter 2, we will give a brief background on regularization theory necessary for explaining our work on surface reconstruction. Chapter 3 presents the invariant energy functionals employed for regularization. Chapter 4 describes how preservation of discontinuities is achieved using our new energy functional with the use of positionally unbiased derivative estimates. A computationally efficient way of computing the volume between two surfaces normalized by surface area as an invariant measure for comparing the surface reconstruction results is presented in chapter 5. Curve reconstruction will be described in chapter 6 by obtaining one dimensional analogs similar to the equations derived for surface reconstruction. In chapter 7, experimental results will be given for both synthetic and actual range data.

Chapter 2

Regularization for surface reconstruction

Regularization is a mathematical technique used to solve ill-posed problems that imposes smoothness constraints on possible solutions. In this chapter, we will briefly describe on regularization theory employed for our surface reconstruction work.

Let an object have the parametric representation $\vec{r}(\mathbf{u}) = (x(u, \mathrm{v}), \mathrm{y}(\mathrm{u}, \mathrm{v}), z(u, \mathrm{v}))$, u = (u, v) **C** R^2. Given a set of noise corrupted data, D = $\left\{c_{i,j} | c_{i,j} = (c^x_{i,j}, c^y_{i,j}, c^z_{i,j})\right\}$ from which we recover the solution $\vec{r}(\mathbf{u})$, we define an energy function $E(\vec{r}(\mathbf{u}), \mathrm{D})$ which measures the compatibility between the solution and the sampled data,

$$E(\vec{r}(\mathbf{u}), D) = \sum_{c_{i,j} \in D} \rho(I[\vec{r}(\mathbf{u})], c_{i,j})$$

where (i, j) is the measurement location in u and ρ is an appropriate metric which is zero at (i, j) where no data is given. D provides shape estimates which consist of constraints on location and/or surface normal at specific points on the surface. Thus, the measurement functional, **I** will have one of the following forms,

$$\begin{aligned} I[\vec{r}(u, v)] &= \vec{r}(u_i, v_j) \\ I[\vec{r}(u, v)] &= \frac{\vec{r}_u(u_i, v_j) \times \vec{r}_v(u_i, v_j)}{||\vec{r}_u(u_i, v_j) \times \vec{r}_v(u_i, v_j)||} \end{aligned}$$

where (u_i, v_j) is a location where a measurement is recored, and $\vec{r}_u(\mathbf{u})$, $\vec{r}_v(\mathbf{u})$ represents the derivative of the vector with respect to the parameter, u and v respectively. The first form is a positional constraint, while the second is a constraint on the local surface normal.

A stabilizing function $E_p(\vec{r}(\mathbf{u}))$ which embodies the desired smoothness constraints is added and the solution $\vec{r}^*(\mathbf{u})$ that minimizes the total energy (2.1) is found.

$$E^{\lambda}(\vec{r}(\mathbf{u})) = E(\vec{r}(\mathbf{u}), \mathrm{D}) + \lambda^2 E_p(\vec{r}(\mathbf{u})) \tag{2.1}$$

The regularization paramenter λ controls the amount of smoothing performed.

In order to define an invariant stabilizer, an invariant characteristic of the surface is integrated over the surface to form a measure of surface consistency. The measure is defined so that the more consistent the surface is with our ideal model of a reconstructed surface, the smaller its value. The following is an example of a first order invariant stabilizing function that represents the small deflection energy of a surface:

$$E_p(\vec{r}(\mathbf{u})) \;=\; \int_{\Omega} \|\vec{r}_u(\mathbf{u}) \times \vec{r}_v(\mathbf{u})\| d\mathbf{u} \tag{2.2}$$

Ω C R^2 denotes the image domain. This stabilizer, however, is not convex, making the solution using (2.2) computationally expensive.

The explicit form can be thought of as a special case of the parametric **form** that is;

$$x(u,v) = x \quad y(u,v) = y \quad and \quad \vec{r}(x,y) = (x, y, z(x,y)).$$

When the Euclidean metric is used, the metric ρ for the data compatibility term becomes,

$$\rho = (z(x_i, y_j) - c^z_{i,j})^2 + (x_i - c^x_{i,j})^2 + (y_j - c^y_{i,j})^2 \tag{2.3}$$

Although this metric is invariant, its practical application often requires that

$$x_i = c^x_{i,j} \quad and \quad y_j = c^y_{i,j},$$

resulting in

$$\rho = |z(x_i, y_j) - c^z_{i,j}| \quad or \quad (z(x_i, y_j) - c^z_{i,j})^2 \tag{2.4}$$

which is not invariant with respect to rotations of the coordinate system.

When the explicit form is used, equation (2.2) is expressed as

$$E_p(\mathbf{z}) \;=\; \int\int_{\Omega} (\sqrt{1 + z_x^2 + z_y^2} - 1) dx dy \tag{2.5}$$

A convex approximation to the nonconvex and invariant stabilizing function (2.5) is desired for computational efficiency. The following is a commonly used convex approximation to (2.5), called the membrane model, which assumes $z_x \approx 0$ and $z_y \approx 0$:

$$E_p(\mathbf{z}) \;=\; \int\int_{\Omega} (z_x^2 + z_y^2) dx dy \tag{2.6}$$

To find the minimum energy solution, it is necessary to discretize the domain of the surface using a finite number of nodal variables, $z_{i,j}$. For simplicity, we choose to discretize the problem using finite difference methods, however, finite element analysis is a more flexible approach than the finite difference method. A brief summary of the finite element method that is related to visual surface reconstruction is found in [32]. A number of ***relazation*** methods such as Jacobi, Gauss-Seidel, and simultaneous over-relaxation (SOR) are used to solve the large sparse linear system that results from the overall energy (2.1). Convergence of the Jacobi method (or the method of simultaneous displacement) is usually very slow. The Gauss-Seidel method (or the method of immediate displacement) is faster than the Jacobi method by using the newly updated values in subsequent computations immediately after they become available. The simultaneous over-relaxation (SOR) method is obtained by accelerating the rate of convergence of the Gauss-Seidel method by the so-called ***overrelazation*** parameter. Gauss-Seidel is used by Terzopoulos [30] while SOR is used by Blake and Zisserman [4]. SOR is used for FIT while Gauss-Seidel is used for IDFIT-BIASED and IDFIT-UNBIASED because of the difficulty in determining the ***overrelazation*** parameter. However, the updating equations for the three reconstruction methods are presented in SOR form for ease of comparison. Relaxation has two advantages over direct methods such as Gaussian elimination and LU decomposition. It needs to store only nonzero entries of the system matrix and is readily parallelizable. See [32] and [21] for a brief survey of relaxation methods.

Chapter 3

Viewpoint invariant reconstruction of surfaces

As mentioned in chapter 1, surface reconstruction that is not invariant with respect to viewpoint may produce different symbolic descriptions, resulting in failure to identify an object in a scene. In this chapter, we develop the invariant energy functions that are employed for the data compatibility measure (section 3.1) and the stabilizing function (section 3.2).

If the energy functional E^{A} has a unique global minimum and it is invariant to rotations and transformations of the constraints, then the reconstructed surface will also be invariant. We can easily verify this by considering a collection of constraints D and any surface $\vec{r}(\mathbf{u})$. Invariance of the functional E^{A} implies that

$$E^{\lambda}(\vec{r}(\mathbf{u}), \mathrm{D}) = E^{\lambda}(\vec{r}^{*}(\mathbf{u}), \mathrm{D}^{*})$$

where $\vec{r}^{*}(\mathbf{u})$ and D* denote the rotated and translated surface and constraints respectively. Then

$$E^{\lambda}(\vec{r}_1(\mathbf{u}), \mathrm{D}) = \inf_{\vec{r}(\mathbf{u})} E^{\lambda}(\vec{r}(\mathbf{u}), \mathrm{D}) = \inf_{\vec{r}^{*}(\mathbf{u})} E^{\lambda}(\vec{r}^{*}(\mathbf{u}), \mathrm{D}^{*}) = E^{\lambda}(\vec{r}_2(\mathbf{u}), \mathrm{D}^{*})$$

Since E^{A} has a unique global minimum,

$$\vec{r}_1(\mathrm{u}) = \vec{r}_2(\mathbf{u}).$$

Then, the surface reconstruction algorithm will be invariant to rotations and translations. The invariance of E^{A} can be achieved by finding an invariant stabilizer and an invariant metric on the constraint space.

3.1 Invariant metric on D

The depth constraint data in the explicit form is used in our work. As pointed out in chapter 1, the commonly used metric (2.4) is not invariant to rotations. Unfortunately, the invariant metric (2.3) cannot be used unless one uses the parametric form of energy [27]. When the parametric form is employed, the same reconstruction process must be carried out for each x, y, and z component in order to obtain the reconstruction result, making this approach computationally expensive. Fortunately, for the explicit form, the perpendicular distance $|z - c|cos\phi$ is invariant under the assumption that the surface, z and the constraint surface, c are roughly parallel, where $cos\phi$ is the surface slant [2]. The squared distance, $(z - c)^2 cos^2\phi$, which is also invariant is used in our work. The data compatibility term $E(z, D)$ is as follows. For surface reconstruction,

$$\begin{aligned} E(z,D) &= \textstyle\sum_{i,j}(z_{i,j} - c_{i,j})^2 cos^2\phi \\ &= \textstyle\sum_{i,j}(z_{i,j} - c_{i,j})^2 \frac{1}{1+z_x^2+z_y^2} \end{aligned} \tag{3.1}$$

where z, and z_y are the first order derivative at the location of (i,j). The estimates, $\hat{z_x}$ and $\hat{z_y}$ of z_x and z, are inserted as constants in the computation.

Equation (3.1) describes our assumption about the noise in range images saying that noise is greater in regions with high slope. This noise model can be justified by the result reported in [13] claiming that the larger the angle between the surface normal and the illuminator direction of a light stripe range finder, the larger uncertainty exists in the sensed z value.

3.2 Approximately invariant first order stabilizing function

We present a first order stabilizing function that is both convex and approximately invariant by examining Taylor expansions of the invariant stabilizing function (2.5) which are different from the first order expansion used for the membrane model (2.6). Figure 3.1 shows the approximation errors when the first, second, third, and fourth order Taylor expansions are employed respectively to approximate the invariant stabilizing function (2.5). The membrane model approximation (2.6) to the invariant stabilizing function (2.5) is a reasonable choice because it gives a smaller approximation error than higher order expansions as the slope, $z_x^2 + z_y^2$, increases. But the approximation error of first order expansion is not ignorable when

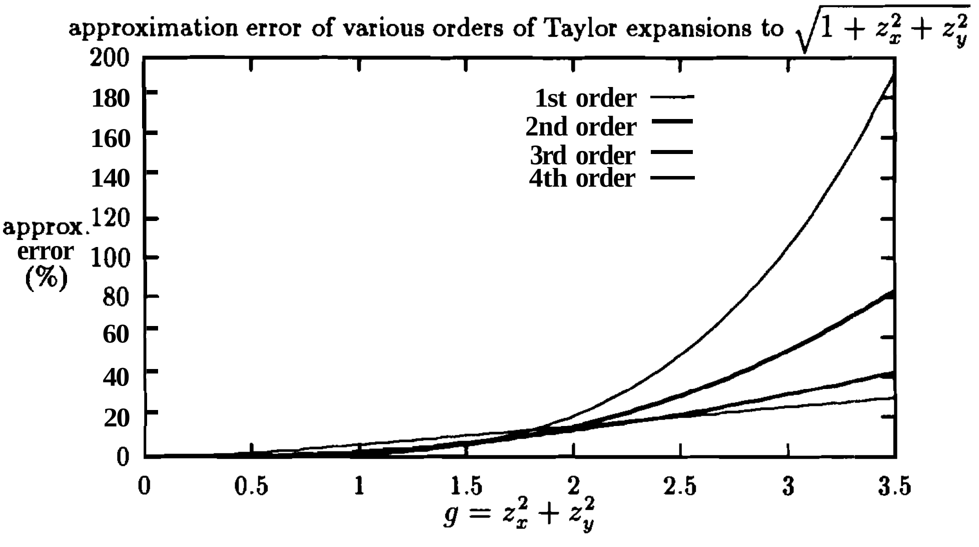

Figure 3.1: approximation errors for various orders of Taylor expansions

the slope, $z_x^2 + z_y^2$ is large, i.e. surfaces of an image are steep. Our goal is to reduce this approximation error. One obvious choice is to use a higher order expansion of Taylor series at g $= \hat{g}$. If we can come up with a reliable estimate of $\hat{g}$ over an image, where g is $z_x^2 + z_y^2$ and $\hat{g}$ is its estimate, then we can reduce the approximation error and achieve an invariant function. However, employing a high order expansion not only produces a nonlinear system but also causes approximation error to be amplified in those higher order terms. The error is especially pronounced in noisy situations. Therefore, our choice of approximation is to use a first order expansion of the Taylor series at g $= \hat{g}$ instead of at g $= 0$. The approximation becomes:

$$\begin{aligned}
&\sqrt{1+z_x^2+z_y^2}\ |_{\ at\ z_x^2+z_y^2\ =\ \hat{g}} \\
&\approx \sqrt{1+\hat{g}} + \frac{1}{2\sqrt{1+\hat{g}}}(z_x^2+z_y^2-\hat{g}) \\
&= \frac{1}{2\sqrt{1+\hat{g}}}(z_x^2+z_y^2) + \sqrt{1+\hat{g}} + \frac{\hat{g}}{2\sqrt{1+\hat{g}}} \qquad (3.2)
\end{aligned}$$

IDFIT-BIASED and IDFIT-UNBIASED employ a stabilizing function using (3.2). The performance of IDFIT-BIASED and IDFIT-UNBIASED with respect to invariance will be better than FIT because their stabilizing functions better approximate the invariant energy (2.5) than the stabilizer (2.6) of FIT. The stabilizing functions used for IDFIT-BIASED and IDFIT-UNBIASED reduce the approximation error to the energy (2.5) when $z_x^2 + z_y^2$ is large, i.e., surfaces of an image are steep. This theoretical performance difference with respect to invariance will be verified in the result section.

Chapter 4

Discontinuity-preserving reconstruction of surfaces

In this chapter, we present how preservation of discontinuities and robustness to the smoothing parameter λ are achieved using our new energy functional. Section **4.1** describes the discretized form of the energy functional and two basic schemes of estimating derivatives (biased and unbiased). The effect of the two different methods of estimating derivatives on the reconstruction results is presented in section **4.2** and **4.3.** We start this chapter with a brief review of the previous research on discontinuity-preserving surface reconstruction.

Many researchers have attempted to reconstruct surfaces with sharp preservation of discontinuities [26] [23] [22] [6] [34] [20] [32] [31]. In most of this work, preservation of discontinuities is achieved by properly choosing weighting functions by which the adjacent pixels that are more likely to belong to different regions are less or not weighted in the computation of a reconstructed pixel value. For spline based methods, the equivalent idea is to weight the basis functions in a similar fashion. However, these approaches do not consider invariance of the reconstruction result at the same time. Cubic spline fitting was used by Stevenson and Delp [26]. They conceived discontinuities as a deviation from the smoothness assumption and used the theory of robust statistics to deal with outliers. The form of stabilizing function was changed by a weighting function which varies quadratically for values below the threshold and linearly for values above the threshold. A Huber minirnax function [12] was used as a convex weight function. Blake and Zisserman's [2] [4] energy function was not derived in the same fashion as in Stevenson and Delp' s work, but the effect is similar in that a quadratic and a constant weighting function resulted below and above a threshold respectively. Unfortunately, the resulting functional minimization problem is nonconvex. The GNC (Graduated NonConvex) algorithm, which is a deterministic algorithm and equivalent to the Mean Field algorithm [9], was used to solve the minimization problem. However the computation is expensive like other techniques that minimize nonconvex functionals and is not guaranteed to find the global minimum. Sinha and Schunck [23] [22] used a weighted B-spline in order to achieve preservation of discontinuities. B-splines are weighted according to the gradient values. The current work presented here extends the work of Yi and Chelberg [34] by including reconstruction of curves and investigating the property of robustness to the smoothing parameter λ as well. The idea of anisotropic diffusion using divergence was employed in Perona and Malik's work [20]. It is a first order model without a data compatibility measure and the invariance property was not considered. In Perona and Malik's work [20], $e^{-(\|\nabla Z\|/K^2)}$ and $\frac{1}{1+(\frac{\|\nabla Z\|}{K})^2}$($K$ is a constant) are adopted as weights. VZ are computed by $z_{i-1,j} - z_{i,j}$, $z_{i+1,j} - z_{i,j}$, $z_{i,j+1} - z_{i,j}$, and $z_{i,j-1} - z_{i,j}$ for four adjacent pixels in North, South, East, and West directions respectively. In contrast, our weighting function will be presented in the following section as $\frac{1}{\sqrt{1+\nabla Z}}$ where VZ represents an estimate of squared gradient at each adjacent pixel's location. We recommend the use of our weighting scheme when both invariance and preservation of discontinuities are desired because our weighting function is obtained by explicitly considering the invariance property. Terzopoulos [31] used a mixture of membrane model and plate model with continuity-control weighting functions. The idea was basically to inhibit smoothing across discontinuity boundaries. Discontinuities are introduced gradually at the locations of high curvature during iterative reconstruction of a piecewise-continuous surface. Invariance was not considered and determination of the threshold values in each iteration appears to be difficult.

4.1 The discrete equations

For simplicity, we will use the following ***forward finite difference*** in order to approximate the continuous surface although it is possible to discretize it using a variety of finite elements.

$$\hat{z}_x = \frac{1}{h_x}(z_{i,j+1} - z_{i,j}) \quad \text{and} \quad \hat{z}_y = \frac{1}{h_y}(z_{i+1,j} - z_{i,j}). \tag{4.1}$$

This discretization follows a regular Cartesian sampling pattern typical of images. The image domain $\Omega \subset \Re^2$ is tessellated into rectangular subdomains with sides of h_x and $h,$ in the x and y directions respectively. Nodes are located at subdomain corners where they are shared by adjacent subdomains.

Combining the stabilizing function and the data compatibility measure described in the previous section, we obtain

$$
\begin{aligned}
E^{\lambda}(\mathbf{z}) &= \sum_{i,j} l_{i,j}\frac{1}{1+\hat{g}_{i,j}}(z_{i,j}-c_{i,j})^2 \\
&+ \lambda^2 \int\int_{\Omega}\left\{\frac{1}{\sqrt{1+\hat{g}}}(z_x^2+z_y^2)+2\sqrt{1+\hat{g}}+\frac{\hat{g}}{\sqrt{1+\hat{g}}}-1\right\}dxdy \qquad (4.2)
\end{aligned}
$$

where $\hat{g}_{i,j}$ is the estimate of $z_x^2 + z_y^2$ at the location of node (i, j) and $l_{i,j}$ is zero where no data is provided at the location of (i, j). We get the following energy form by discretizing the energy (4.2) using the finite difference (4.1).

$$
\begin{aligned}
E^{\lambda}(\mathbf{z}) &= \sum_{i,j} l_{i,j}\frac{1}{1+\hat{g}_{i,j}}(z_{i,j}-c_{i,j})^2 \\
&+ \lambda^2 \sum_{i,j}\frac{1}{\sqrt{1+\hat{g}_{i,j}}}\left\{\frac{1}{h_x^2}(z_{i,j+1}-z_{i,j})^2+\frac{1}{h_y^2}(z_{i+1,j}-z_{i,j})^2\right\}. \qquad (4.3)
\end{aligned}
$$

where the constant terms in (4.2) are ignored. The resulting SOR updating equations for inside pixels are as follows.

If there is data at node (i, j),i.e, $l_{i,j}=1$,

$$
\begin{aligned}
z_{i,j}^{n+1} &= z_{i,j}^{n} - \frac{\omega}{a+b\lambda^2}[(a+b\lambda^2)z_{i,j}^{n} - \frac{1}{1+\hat{g}_{i,j}}c_{i,j} \\
&-\lambda^2\left(\frac{z_{i,j-1}^{n+1}}{h_x^2\sqrt{1+\hat{g}_{i,j-1}}}+\frac{z_{i-1,j}^{n+1}}{h_y^2\sqrt{1+\hat{g}_{i-1,j}}}+\frac{z_{i,j+1}^{n}}{h_x^2\sqrt{1+\hat{g}_{i,j}}}+\frac{z_{i+1,j}^{n}}{h_y^2\sqrt{1+\hat{g}_{i,j}}}\right)] \qquad (4.4)
\end{aligned}
$$

otherwise, i.e, $l_{i,j}=0$,

$$
z_{i,j}^{n+1} = z_{i,j}^{n} - \frac{\omega}{b}[bz_{i,j}^{n} - \left(\frac{z_{i,j-1}^{n+1}}{h_x^2\sqrt{1+\hat{g}_{i,j-1}}}+\frac{z_{i-1,j}^{n+1}}{h_y^2\sqrt{1+\hat{g}_{i-1,j}}}+\frac{z_{i,j+1}^{n}}{h_x^2\sqrt{1+\hat{g}_{i,j}}}+\frac{z_{i+1,j}^{n}}{h_y^2\sqrt{1+\hat{g}_{i,j}}}\right)] \qquad (4.5)
$$

where a $= \frac{1}{1+\hat{g}_{i,j}}$, $b = \frac{1}{h_x^2\sqrt{1+\hat{g}_{i,j}}} + \frac{1}{h_y^2\sqrt{1+\hat{g}_{i,j}}} + \frac{1}{h_x^2\sqrt{1+\hat{g}_{i,j+1}}} + \frac{1}{h_y^2\sqrt{1+\hat{g}_{i+1,j}}}$ and w is the overrelaxation parameter of the SOR method. The SOR updating equations when the ordinary membrane (2.6) is used are found in [3].

Given a novel form of the energy function (4.3), another problem faced is how to estimate the gradient, $\hat{g}_{i,j} = \hat{z}_x^2 + \hat{z}_y^2$ at the location of node (i, j). This problem can be conceived as a tuning problem because the reconstruction performance may degrade on the disagreement of the weighting pattern of the updating equation with the method of estimating the derivative. Two basic schemes that are commonly used are as follows. One is the forward difference which is a biased estimate of the derivative. It computes $\hat{z}_x$ and $\hat{z}_y$ at the location of (i, j) as

$$
\hat{z}_x = \frac{1}{h_x}(z_{i,j+1}-z_{i,j}) \quad \text{and} \quad \hat{z}_y = \frac{1}{h_Y}(z_{i+1,j}-z_{i,j}). \qquad (4.6)
$$

This is the scheme used in the discretization of the energy (4.2). Another estimate that is not biased is the central difference obtained as

$$\hat{z}_x = \frac{1}{2h_x}(z_{i,j+1} - z_{i,j-1}) \quad \text{and} \quad \hat{z}_y = \frac{1}{2h_y}(z_{i+1,j} - z_{i-1,j}). \tag{4.7}$$

In the next two subsections, we will investigate the preservation of discontinuities and overall reconstruction performance for two alternative reconstruction methods in order to see how these two different method of estimating the derivative affect the reconstruction results. One method is the use of the biased derivative estimate (4.6) for the energy (4.3). The other method is the use of the unbiased derivative estimate (4.7) with an appropriate adjustment of the energy (4.3) for the purpose of preservation of discontinuities. In short, the latter is the recommended method for surface reconstruction.

4.2 Preservation of discontinuities

The energy function (4.3) will be investigated in this section for discontinuity-preserving reconstruction. A weighted sum of four adjacent pixels should be chosen such that the pixels adjacent to discontinuities are weighted less than those further away in order to sharply preserve discontinuities. The estimates, $\hat{z}_x$ and $\hat{z}_y$ computed from the reconstruction result using the ordinary membrane model (2.6) are provided for the second reconstruction that achieves both invariance and preservation of discontinuities.

It is easy to see that the biased estimate (4.6) is more appropriate than the unbiased estimate (4.7) for the purpose of preservation of discontinuities when the updating equations (4.4) and (4.5) from the energy (4.3) are adopted for reconstruction of surfaces. Figure 4.1 shows a simple example where the weighting pattern in the case of the biased estimate (4.6) will more sharply preserve discontinuities than in the case of the unbiased estimate (4.7) when the updating equations (4.4) and (4.5) from the energy (4.3) are used. In the case of the unbiased estimate (4.7), uniform averaging of the adjacent nodal values occurs resulting in blurring across discontinuities. Simply put, if the updating equation for the case of $l_{i,j} = 0$ and the Guass Seidel algorithm ($w = 1$) is considered, the updated value of the current node at (i, j) in Figure 4.1 (b) is 0.62 whereas the updated value is 1.25 in Figure 4.1 (a). To insure sharp preservation of discontinuities, this value should be as close to zero as possible.

When unbiased estimates (4.7) are used with the energy form (4.3), however, the asymmetrical distribution of weighting pattern around the node to be updated in the equations (4.4)

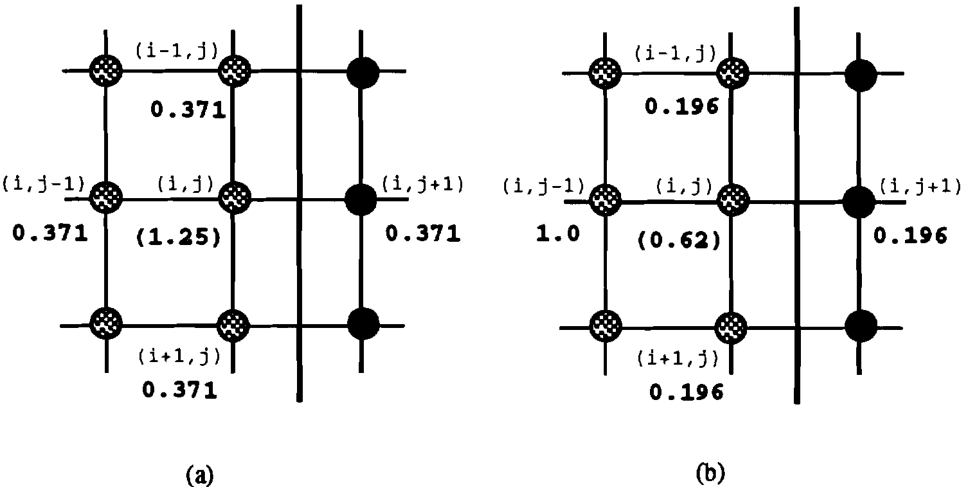

Figure 4.1: A straight step edge with the edge magnitude of 5 is represented as a thick line. The textured circles denote the nodes with data value 0 and the dark circles the nodes with data value 5. The weights are shown in bold and the updated node value in parenthesis. When the updating equations (4.4) and (4.5) are used, (a) the weighting pattern for the unbiased estimate (4.7) and (b) the weighting pattern for the biased estimate (4.6) are illustrated. Perfect reconstruction would yield a value of 0 at (i, j).

and (4.5) is not optimal for the purpose of preservation of discontinuities. Note that $z^n_{i,j+1}$ and $z^n_{i+1,j}$ are weighted by the gradient information at (i, j) which is not the gradient information at their own locations. Figure 4.2 illustrates a simple example where the asymmetrical weighting pattern is not optimal. When this asymmetric weighting pattern from the updating equations (4.4) and (4.5) is used with (4.7) in Figure 4.2, all four weights are the same, resulting in blurring at the current node. We resolve this problem by using $\hat{g}_{i,j+1} \approx \hat{g}_{i,j}$ and $\hat{g}_{i+1,j} \approx \hat{g}_{i,j}$ assuming a smooth surface. Then the energy becomes

$$\begin{aligned} E^\lambda(\mathbf{z}) &= \textstyle\sum_{i,j} l_{i,j} \frac{1}{1+\hat{g}_{i,j}} (z_{i,j} - c_{i,j})^2 \\ &+ \lambda^2 \{ \cdots + \frac{(z_{i,j+1}-z_{i,j})^2}{h_x^2\sqrt{1+\hat{g}_{i,j+1}}} + \frac{(z_{i+1,j}-z_{i,j})^2}{h_y^2\sqrt{1+\hat{g}_{i+1,j}}} + \frac{(z_{i,j}-z_{i,j-1})^2}{h_x^2\sqrt{1+\hat{g}_{i,j-1}}} + \frac{(z_{i-1,j}-z_{i,j})^2}{h_y^2\sqrt{1+\hat{g}_{i-1,j+1}}} + \cdots \} \end{aligned} \tag{4.8}$$

The convexity property is not changed because the energy is still expressed as a sum of positive squared terms. The resulting SOR updating equations for the inside pixels are as follows:

If there is data at node (i,j),i.e, $l_{i,j} = 1$,

$$\begin{aligned} z^{n+1}_{i,j} &= z^n_{i,j} - \frac{\omega}{a+b\lambda^2} [(a + b\lambda^2) z^n_{i,j} - \frac{1}{1+\hat{g}_{i,j}} c_{i,j} \\ &\quad -\lambda^2 (\frac{z^{n+1}_{i,j-1}}{h_x^2\sqrt{1+\hat{g}_{i,j-1}}} + \frac{z^{n+1}_{i-1,j}}{h_y^2\sqrt{1+\hat{g}_{i-1,j}}} + \frac{z^n_{i,j+1}}{h_x^2\sqrt{1+\hat{g}_{i,j+1}}} + \frac{z^n_{i+1,j}}{h_y^2\sqrt{1+\hat{g}_{i+1,j}}})] \end{aligned} \tag{4.9}$$

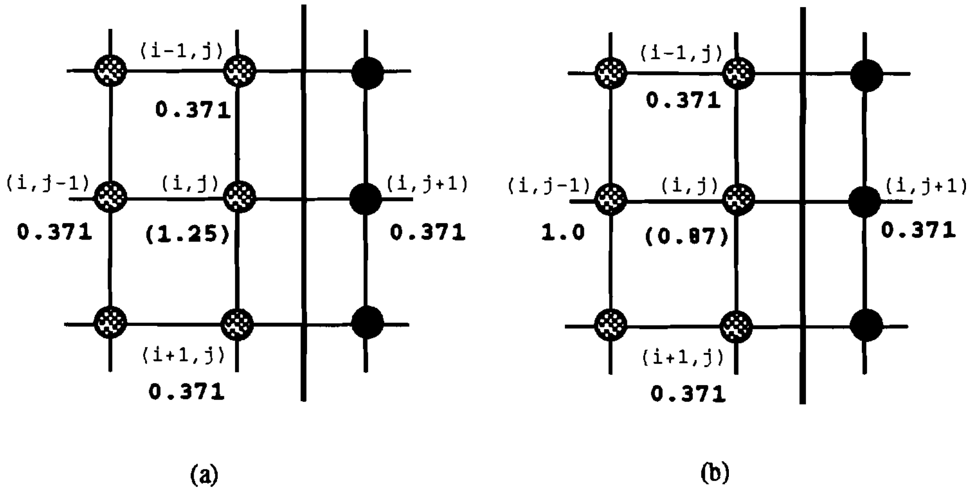

Figure 4.2: A straight step edge with the edge magnitude of 5 is represented as a thick line. The textured circles denote the nodes with data value 0 and the dark circles the nodes with data value 5. The weights are shown in bold and the updated node value in parenthesis. When the unbiased estimates (4.7) are used, (a) the weighting pattern for the updating equations (4.4) and (4.5), (b) the weighting pattern for the updating equations (4.9) and (4.10)

otherwise, i.e, $l_{i,j} = 0$,

$$z^{n+1}_{i,j} = z^n_{i,j} - \frac{\omega}{b}[bz^n_{i,j} - (\frac{z^{n+1}_{i,j-1}}{h_x^2\sqrt{1+\hat{g}_{i,j-1}}} + \frac{z^{n+1}_{i-1,j}}{h_y^2\sqrt{1+\hat{g}_{i-1,j}}} + \frac{z^n_{i,j+1}}{h_x^2\sqrt{1+\hat{g}_{i,j+1}}} + \frac{z^n_{i+1,j}}{h_y^2\sqrt{1+\hat{g}_{i+1,j}}})] \qquad (4.10)$$

where a $= \frac{1}{1+\hat{g}_{i,j}}$, $b = \frac{1}{h_y^2\sqrt{1+\hat{g}_{i-1,j}}} + \frac{1}{h_y^2\sqrt{1+\hat{g}_{i+1,j}}} + \frac{1}{h_x^2\sqrt{1+\hat{g}_{i,j-1}}} + \frac{1}{h_x^2\sqrt{1+\hat{g}_{i,j+1}}}$. If the updating equation for the case of $l_{i,j} = 0$ and the Guass Seidel algorithm ($w = 1$) is considered, the updated value of the current node at (i, j)in Figure 4.2 (b) is 0.87 whereas the updated value is 1.25 in Figure 4.2 (a). We state here again the three reconstructions to be compared that are introduced in chapter 1.

- FIT : ordinary reconstruction using the ordinary membrane model (2.6)
- IDFIT-BIASED : invariant and discontinuity-preserving reconstruction using the updating equations (4.4) and (4.5) with the biased estimates (4.6)
- IDFIT-UNBIASED :invariant and discontinuity-preserving reconstruction using the updating equations (4.9) and (4.10) with the unbiased estimates (4.7)

IDFIT-UNBIASED is our choice for reconstruction of surfaces because its reconstruction (IDFIT-UNBIASED) not only achieves both invariance and preservation of discontinuities but also is robust with respect to the smoothing parameter λ. The property of robustness to the smoothing parameter λ will be described in the following section.

We have computed the weighting patterns of the edge pixels for the cases of IDFIT-BIASED and IDFIT-UNBIASED for various patterns of discontinuities. A simple example of this was illustrated in Figure **4.1** (b) and Figure **4.2** (b). The comparison of the weighting patterns for the edge pixels may lead to a careless conclusion that IDFIT-BIASED is better at preservation of discontinuities than IDFIT-UNBIASED because, in Figure **4.1** (b) and Figure **4.2** (b), the updated value of the current node (edge pixel) for IDFIT-BIASED and IDFIT-UNBIASED is **0.62** and **0.87** respectively for the same image. However, the weighting patterns of the pixels next to the edge pixels plays a more important role than those of the edge pixels in overall reconstruction performance as well as in the reconstruction of pixel values at the edge locations. In short, IDFIT-UNBIASED produces less reconstruction error than IDFIT-BIASED due to the reasons to be described in section **4.3.**

Both IDFIT-UNBIASED and IDFIT-BIASED perform better than FIT. All three methods reconstruct a surface by averaging neighboring pixel values. IDFIT-UNBIASED and IDFIT-BIASED employ a weighted averaging scheme so that neighbor pixels that are more likely to belong to different regions are less weighted in computation while FIT uses averaging of neighboring pixel values without an appropriate weighting.

4.3 Robustness

A. Robustness to directions of discontinuities

We have evaluated the reconstruction performance of FIT, IDFIT-BIASED, and IDFIT-UNBIASED as the direction of a step discontinuity is varied from **0°** to **90°** with respect to the horizontal direction. Figure **4.3** shows the result using an **11** x **11** image array where the discontinuity contrast was **10.0.** The performance of the three reconstruction methods, FIT, IDFIT-BIASED, and IDFIT-UNBIASED does not show much difference with respect to robustness to direction of discontinuity. However, their performance at each direction shows that IDFIT-BIASED and IDFIT-UNBIASED are much better than FIT and IDFIT-BIASED performs worse than IDFIT-UNBIASED. Based on the results of section **4.1,** we could expect that the performance of IDFIT-BIASED and IDFIT-UNBIASED would be better than FIT because of the use of weighted vs. unweighted averaging of the neighbor nodes. The reason

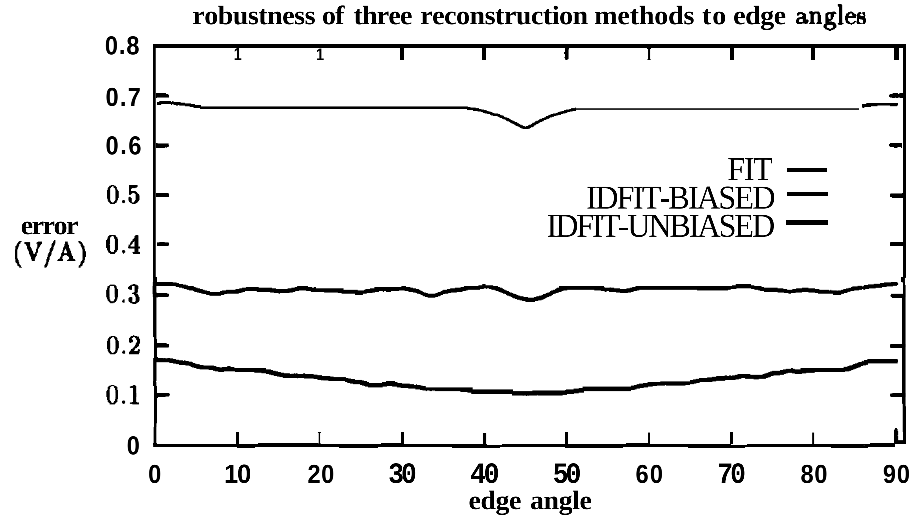

Figure **4.3:** The performance of FIT, IDFIT-BIASED, and IDFIT-UNBIASED for various directions of discontinuity

why IDFIT-UNBIASED performs better than IDFIT-BIASED will be described immediately in the following section. This performance result will be verified for the test images used in the experiments presented in the result section.

B. Robustness to the oothing aram ter λ

Figure 4.4 shows a simple example for the purpose of explaining why IDFIT-UNBIASED performs better than IDFIT-BIASED. This example can be considered as one data point of Figure **4.3** for which the direction of discontinuity is 90°. The main role is played by the nodes (textured circles) next to the edge nodes (filled circles). Figure 4.4 (c) (d) shows the weighting pattern for the neighbor nodes of the current node $z_{i,j}$ (textured. circle) for the algorithms **IDFIT-BIASED(c)** and **IDFIT-UNBIASED(d)** respectively. When the edge node $z_{i,j+1}$ (filled circle) is blurred during reconstruction, the blurring effect propagates to the neighboring nodes. When the current node $z_{i,j}$ is updated at the next iteration, different weighting patterns of IDFIT-BIASED and IDFIT-UNBIASED for the neighbor nodes of $z_{i,j}$ make a difference in determining how much blurring effect $z_{i,j}$ will get from $z_{i,j+1}$. In the case of IDFIT-BIASED, the blurred edge node $z_{i,j+1}$ has full effect on $z_{i,j}$ when $z_{i,j}$ is updated because of the uniform weighting pattern of IDFIT-BIASED for the neighboring nodes of $z_{i,j}$. On the other hand, $z_{i,j}$ of IDFIT-UNBIASED get much less blurring effect from $z_{i,j+1}$ than

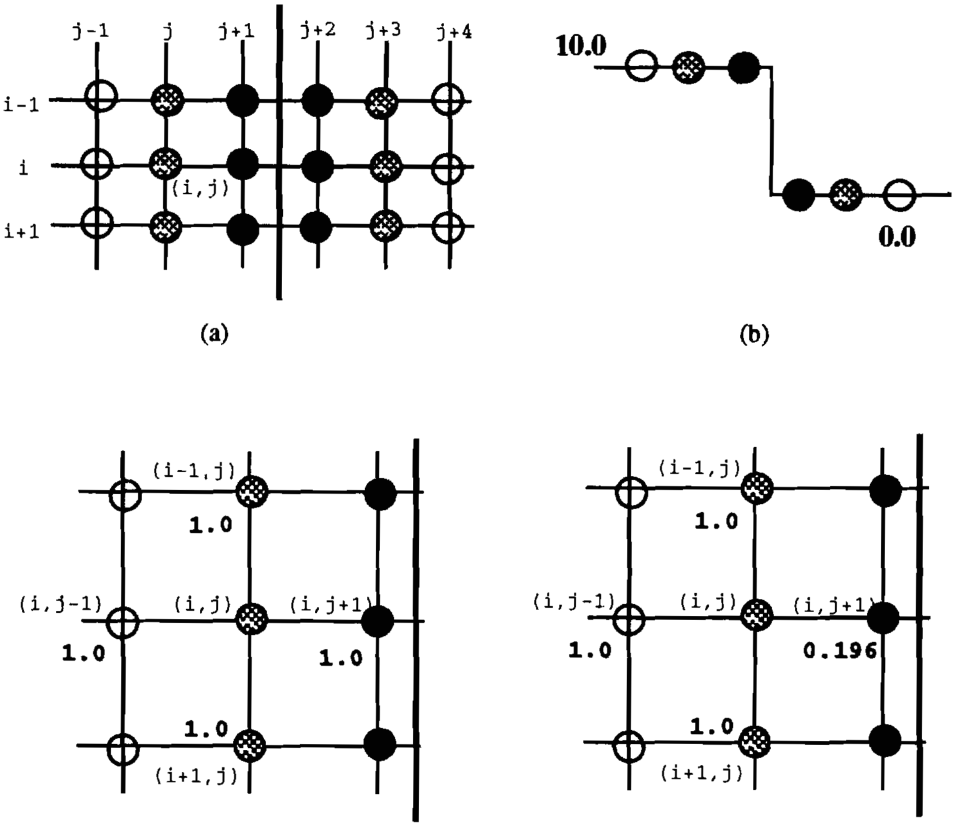

(a)

(b)

(c)

(d)

Figure 4.4: (a) an image array where the thick line represents a straight step discontinuity with magnitude of 10.0 (b) i-th row of the image (c) weighting pattern (weights in bold) in the case of IDFIT-BIASED (d) weighting pattern (weights in bold) in the case of IDFIT-UNBIASED

would be the case for $z_{i,j}$ of IDFIT-BIASED. Notice that this effect continues to propagate to the immediate four neighbors of $z_{i,j}$ and all the other nodes in the sequel. The updated node $z_{i,j}$ has an effect on the edge node $z_{i,j+1}$ when $z_{i,j+1}$ is updated at the next iteration. The edge nodes of IDFIT-UNBIASED can maintain sharper contrast than those of IDFIT-BIASED because the the nodes next to the edge nodes are less blurred in the previous iteration in the case of IDFIT-UNBIASED than IDFIT-BIASED. This local phenomenon propagates throughout the entire image and this is the reason for the better reconstruction.of IDFIT-UNBIASED than that of IDFIT-BIASED. This ***self-tuning*** like behavior is responsible for the robustness property of IDFIT-UNBIASED to the smoothing parameter λ as well. The same behavior is observed for other directions of discontinuity as seen in the results of Figure 4.3. The robustness to λ of IDFIT-UNBIASED allows the free choice of the smoothing parameter λ without struggling to determining the λ that provides the best reconstruction. Much effort has been devoted to computing an optimal scale parameter λ for other algorithms. Various ways of choosing an optimal λ in the case of quadratic regularization criteria were discussed [33]. Our method avoids these difficulties.

Chapter 5

Invariant measure of the difference between two surfaces

In this chapter, we present a computationally efficient way of computing the volume between two surfaces normalized by the surface area as an invariant measure for comparing surface reconstruction results.

A good quantitative measure for comparing reconstruction results should have several properties. The measure must be invariant with respect to an arbitrary coordinate system. If a measure is not invariant with respect to a coordinate system, then it is possible to obtain inconsistent performance measures. For example, two reconstruction methods A and B are to be compared. Suppose that a surface is reconstructed by methods A and B in two different coordinate systems. A noninvariant performance measure may lead to a conclusion that method A is better than method B in one coordinate system but is worse in the other coordinate system. It is also desirable to use a measure that produces consistent results for different sizes of images. Finally, the value of the measure should be able to be computed simply and efficiently with reasonable accuracy. We propose the volume between two surfaces normalized by the surface area as an invariant measure for comparing reconstruction results. In addition, we present a computationally simple and efficient method of computing the volume between two surfaces and the surface area. The time complexity of our method to compute the volume and the area is O(number of pixels).

The metrics induced by the L^1, L^2 or L^{oo} norms have been popularly usecl in order to give a quantitative measure for comparison of reconstruction results. The use of these metrics has often naturally resulted because some reconstruction methods employ minimization techniques of L^1, L^2 or L^∞ error between the true or target data set and the measurement data set (constraints) to compute the reconstruction results. In Chu and Bovik's work [8], the reconstruction results were computed by minimizing the L'' error (maximum absolute error) and the normalized L^1 (average absolute error) and L'' error were used as performance measures. On the other hand, the L^2 metric has mostly been used as a reasonable performance measure irrespective of reconstruction methods [27] [18] [22]. L^2 and L'' measures were computed in [27]. Sinha and Schunck [22] employed a RMS error measure which is the normalized L^2 metric for comparison of two different reconstructions. The following is the discrete form of L^1 and L^2 metrics normalized by the number of the sampled points and L'' metric for two functions, f and g in the two dimensional case.

$$
\begin{aligned}
L_d^1 metric &= \frac{1}{nm}\sum_{i=1}^{n}\sum_{j=1}^{m}|f(i,j)-g(i,j)| \\
L_d^2 metric &= \frac{1}{nm}\left[\sum_{i=1}^{n}\sum_{j=1}^{m}\{f(i,j)-g(i,j)\}^2\right]^{\frac{1}{2}} \\
L_d^\infty metric &= \sup_{i,j}|f(i,j)-g(i,j)|
\end{aligned}
$$

where $f(i,j)$ and $g(i,j), i = 1,2,...,n$, $j = 1,2,...,m$ are sampled points of two functions, $f(x,y)$ and $g(x,y)$ respectively. The L^1, L^2 and L'' metrics, however, are not invariant with respect to a coordinate system, resulting in different measures in different coordinate systems. It is clear that if the L^2 metric is used as a difference measure, where the slope is high, the difference value is emphasized more than in flat regions.

In order to compute the volume and the surface area, we approximate each surface patch defined on a rectangular grid defined by $(i,j),(i+1,j),(i,j+1)$ and $(i+1,j+1)$ by the least-square-fit plane obtained from those four points. The the volume, V between two surfaces is computed as follows assuming a (n,m) rectangular grid.

$$
\begin{aligned}
V &= \textstyle\sum_{i=1}^{n-1}\sum_{j=1}^{m-1}\left|\frac{h_x h_y}{4}\left\{z^1_{i,j}+z^1_{i+1,j}+z^1_{i,j+1}+z^1_{i+1,j+1}-(z^2_{i,j}+z^2_{i+1,j}+z^2_{i,j+1}+z^2_{i+1,j+1})\right\}\right| \\
&= \textstyle\frac{h_x h_y}{4}\sum_{i=1}^{n-1}\sum_{j=1}^{m-1}\left|(z^1_{i,j}-z^2_{i,j})+(z^1_{i+1,j}-z^2_{i+1,j})+(z^1_{i,j+1}-z^2_{i,j+1})+(z^1_{i+1,j+1}-z^2_{i+1,j+1})\right|
\end{aligned}
$$

where $z^k_{i,j}, k = 1,2$ represents two surfaces.

The surface area, A is calculated as

$$
A = \textstyle\frac{1}{2}\sum_{i=0}^{n-1}\sum_{j=0}^{m-1}
$$

$$
\sqrt{4h_x^2h_y^2 + h_y^2(-z_{i,j}+z_{i+1,j}-z_{i,j+1}+z_{i+1,j+1})^2 + h_x^2(-z_{i,j}-z_{i+1,j}+z_{i,j+1}+z_{i+1,j+1})^2}
$$

Therefore, the volume between a known surface and its reconstructed surface normalized by the known surface area becomes

$$\frac{V}{A}.$$

Knowing that a reconstructed surface is an approximated surface and the surface shape is ambiguous in regions between pixels, the described method of the least-square-error fit plane approximation gives good estimates of the volume between two surfaces and the area of a surface. The advantage of our method lies in that computation is extremely simple and efficient. See [35] for details.

Chapter 6

Viewpoint invariant and discontinuity-preserving reconstruction of curves

In this chapter, we describe viewpoint invariant and discontinuity-preserving reconstruction of plane curves which is a one dimensional analog of the surface reconstruction method (two dimension) presented in earlier chapters.

Accurate estimates of position and distance along a single slice of range data often need to be made very quickly, for example, in order for a robot arm to align objects in the scene or for a visual inspection system to check weld seams. Reconstruction of curves of the form $z = z(x)$ that achieves viewpoint invariance and preservation of discontinuities will be presented in this chapter. Curve reconstruction is carried out along a direction x where x denotes any direction along a single slice of range data.

The same noise model as in the two dimensional range data for surface reconstruction applies to a single slice of range data for curve reconstruction. That is, more noise is assumed in the high sloped part of the curve. The following is the invariant energy function chosen for the data compatibility term.

$$E(z, D) \;=\; \sum_i (z_i - c_i)^2 \frac{1}{1 + z_x^2} \tag{6.1}$$

where D is a collection of data and x is, again, any direction along which a single slice of data is obtained. c; denotes noise corrupted data at a location i. For the stabilizing function, we approximate the following first order invariant energy which represents a small deflection energy of a string.

$$E_p(\mathbf{z}) = \int_\Omega (\sqrt{1+z_x^2} - 1)dx \tag{6.2}$$

where Ω C R denotes the curve domain. A convex approximation to the nonconvex and invariant stabilizing function (6.2) is desired for computational efficiency. One simple choice is a convex approximation to (6.2) similar to the ordinary membrane approximation (2.6) made for surface reconstruction, assuming $z_x \approx 0$.

$$E_p(\mathbf{z}) = \int_\Omega z_x^2 dx \tag{6.3}$$

The approximation error of (6.3) to (6.2) is not ignorable when z_x^2 is large, i.e., where the curve is steep. By arguments similar to those made in section 3.2, we employ the following stabilizing function for curve reconstruction.

$$\begin{aligned} \sqrt{1+z_x^2} \mid_{at\ z_x^2 = \hat{g}} &\approx \sqrt{1+\hat{g}} + \frac{1}{2\sqrt{1+\hat{g}}}(z_x^2 - \hat{g}) \\ &= \frac{1}{2\sqrt{1+\hat{g}}} z_x^2 + 1 + \hat{g} + \frac{\hat{g}}{2\sqrt{1+\hat{g}}} \end{aligned} \tag{6.4}$$

Combining the stabilizing function (6.4) and the data compatibility measure (6.1), we obtain

$$E^\lambda(\mathbf{z}) = \sum_i l_i \frac{1}{1+\hat{g}_i}(z_i - c_i)^2 + \lambda \int_\Omega \left\{ \frac{1}{\sqrt{1+\hat{g}}} z_x^2 + 2\sqrt{1+\hat{g}} + \frac{\hat{g}}{\sqrt{1+\hat{g}}} - 1 \right\} dx \tag{6.5}$$

where $\hat{g}_i$ is the estimate of z_x^2 at the location of i and I; is zero where no data is provided at the location of i. When the above energy is discretized by the finite difference, z, $= \frac{1}{h}(z_{i+1} - z_i)$, the energy becomes

$$E^\lambda(\mathbf{z}) = \sum_i l_i \frac{1}{1+\hat{g}_i}(z_i - c_i)^2 + \lambda \sum_i \frac{1}{\sqrt{1+\hat{g}_i}} \frac{1}{h^2}(z_{i+1} - z_i)^2 \tag{6.6}$$

where h is the sampling interval in the direction x and the constant terms in (6.5) is ignored. The resulting SOR updating equations for inside pixels are as follows.

If there is data at node i, i.e, 1; $= 1$,

$$z_i^{n+1} = z_i^n - \frac{\omega}{a + b\lambda^2}[(a + b\lambda^2)z_i^n - \frac{1}{1+\hat{g}_i}c_i - \lambda^2(\frac{z_{i-1}^{n+1}}{h^2\sqrt{1+\hat{g}_{i-1}}} + \frac{z_{i+1}^n}{h^2\sqrt{1+\hat{g}_i}})] \tag{6.7}$$

otherwise, i.e, I; $= 0$,

$$z_i^{n+1} = z_i^n - \frac{\omega}{b}[bz_i^n - (\frac{z_{i-1}^{n+1}}{h^2\sqrt{1+\hat{g}_{i-1}}} + \frac{z_{i+1}^n}{h^2\sqrt{1+\hat{g}_i}})] \tag{6.8}$$

where $a = \frac{1}{1+\hat{g}_i}$, $b = \frac{1}{h^2\sqrt{1+\hat{g}_{i-1}}} + \frac{1}{h^2\sqrt{1+\hat{g}_i}}$ and w is again the acceleration parameter.

Initially, the estimate $\hat{z}_x$ computed using *(6.3)* is provided for the invariant and discontinuity-preserving reconstruction. Again, two choices are considered to estimate the derivative $\hat{z}_x$ at the location of i. The following is a biased and an unbiased derivative estimate respectively.

$$\hat{z}_x = \frac{1}{h}(z_{i+1} - z_i) \tag{6.9}$$

$$\hat{z}_x = \frac{1}{2h}(z_{i+1} - z_{i-1}) \tag{6.10}$$

The biased estimate *(6.9)* is the same forward difference scheme used in the discretization of the energy *(6.5)*. It is easy to see that the biased estimate *(6.9)* is more appropriate than the unbiased estimate *(6.10)* for the purpose of preservation of discontinuities when the updating equation *(6.7)* and *(6.8)* from the energy *(6.6)* are adopted for reconstruction of curves. When the unbiased estimate *(6.10)* are used, however, the asymmetrical weighting pattern around the pixel to be updated in the equations *(6.7)* and *(6.8)* is not optimal for the purpose of preservation of discontinuities. Note that z_{i+1}^n is weighted by the slope inforination at i which is not the slope information at its own location. We can make an adjustment to the energy *(6.6)* similar to that made in section 4 so that the new energy can provide the updating equations with a symmetric weighting pattern. The adjusted energy is as follows.

$$E^\lambda(\mathbf{z}) = \sum_i l_i \frac{1}{1+\hat{g}_i}(z_i - c_i)^2 + \lambda^2\{\cdots + \frac{(z_{i+1}-z_i)^2}{h^2\sqrt{1+\hat{g}_{i+1}}} + \frac{(z_i - z_{i-1})^2}{h^2\sqrt{1+\hat{g}_{i-1}}} + \cdots\} \tag{6.11}$$

The convexity property is not changed because the energy is still expressed as a sum of positive squared terms. This energy function with the unbiased derivative estimate *(6.10)* is our choice for curve reconstruction. It will be shown for curve reconstruction that the use of the energy *(6.11)* with the use of the unbiased derivative estimate *(6.10)* not only achieves invariance and preservation of discontinuities, but also robustness to the smoothing parameter λ in the reconstruction results.

The resulting SOR updating equations from *(6.11)* for the pixels which are not end points are as follows:

If there is data at node i, i.e, $l_i = 1$,

$$z_i^{n+1} = z_i^n - \frac{w}{a+b\lambda^2}[(a+b\lambda^2)z_i^n - \frac{1}{1+\hat{g}_i}c_i - \lambda^2(\frac{z_{i-1}^{n+1}}{h^2\sqrt{1+\hat{g}_{i-1}}} + \frac{z_{i+1}^n}{h^2\sqrt{1+\hat{g}_{i+1}}})] \tag{6.12}$$

otherwise, i.e, $l_i = 0$,

$$z_i^{n+1} = z_i^n - \frac{\omega}{b}[bz_i^n - (\frac{z_{i-1}^{n+1}}{h^2\sqrt{1+\hat{g}_{i-1}}} + \frac{z_{i+1}^n}{h^2\sqrt{1+\hat{g}_{i+1}}})] \tag{6.13}$$

where a $= \frac{1}{1+\hat{g}_i}$, $b = \frac{1}{h^2\sqrt{1+\hat{g}_{i-1}}} + \frac{1}{h^2\sqrt{1+\hat{g}_{i+1}}}$.

The area between two curves normalized by the arc length is used as an invariant quantitative measure for comparison of curve reconstruction results. By normalizing the area by the arc length, the value of the measure can be compared for different size of curves. In order to compute the area and the arc length, we approximate a curve segment on each interval h by a linear segment. Then the area, A between two curves is computed as follows assuming a n points on a curve.

$$A = \sum_{i=1}^{n-1} \Delta A_i \tag{6.14}$$

where

$$\Delta A_i = \begin{cases} \frac{h}{2}| \ ^{2} + z_i^2 - z_{i+1}^1 - z_i^1| & \text{if two line segments do not intersect} \\ \frac{h}{2}\left(\left|\frac{(z_i^1)^2-2z_i^1z_i^2+(z_i^2)^2}{z_i^1-z_{i+1}^1-z_i^2-z_{i+1}^2}\right| + \left|\frac{(z_{i+1}^1)^2-2z_{i+1}^1z_{i+1}^2+(z_{i+1}^2)^2}{z_i^1-z_{i+1}^1-z_i^2-z_{i+1}^2}\right|\right) & \text{otherwise} \end{cases} \tag{6.15}$$

and z_i^k, k $= 1,2$ represents two curves.

The arc length, L is calculated as

$$l = \sum_{i=1}^{n-1} \sqrt{(z_{i+1} - z_i)^2 + h^2} \tag{6.16}$$

Therefore, the area between a known curve and its reconstructed curve normalized by the known arc length becomes

$$\frac{A}{L}.$$

Knowing that a reconstructed curve is an approximated curve and curve shape is ambiguous between two sampled points, the described method of approximating each curve segment by a linear segment gives good estimates of the area between two curves and the length of a curve. The advantage of the method lies in that computation is extremely simple and efficient. See [35] for details.

Again for curve reconstruction, we name three reconstructions to be compared as follows.

- FIT: ordinary reconstruction using **(6.3)**
- IDFIT-BIASED: invariant and discontinuity-preserving reconstruction using the updating equations **(6.7)** and **(6.8)** with the biased estimates **(6.9)**

- IDFIT-UNBIASED: invariant and discontinuity-preserving reconstruction using the updating equations **(6.12)** and **(6.13)** with the unbiased estimates **(6.10)**

It will be shown in the result section that our new energy functional with the unbiased derivative estimates for curve reconstruction performs well on sparse noisy data. Portions of the curve with high curvature are well reconstructed even though a first order model is employed.

Chapter 7

Experimental results

In this chapter, we report the performance of our new energy functional for invariance, preservation of discontinuities, and robustness to the smoothing parameter λ on dense and sparse images that are noisy. Results for surface reconstruction will be presented first followed by results for curve reconstruction.

Two synthetic range images and two actual range images are used for surface reconstruction experiments. Strips of these images are taken as input data for curve reconstruction experiments. Figures 7.1, 7.6, and 7.7 are used to test for the discontinuity-preserving property. The curved-inclined image in Figure 7.1 has three flat, two inclined (slope 1 and $\frac{1}{2}$) and two curved surfaces (curvature $\frac{1}{20}$ and \$). $N(0,1)$ is added in the direction of surface normal vector where $N(0,1)$ denotes Gaussian noise with mean 0.0 and standard deviation 1.0. Figure 7.2 shows a section of the curved-inclined image after noise is added. Results showing the robustness of the method to various λ (for the ranges of (0.0 $\sim$ 5.0) and (0.0 $\sim$ 30.0)) are reported using this curved-inclined image for FIT, IDFIT-BIASED, IDFIT-UNBIASED for both surface reconstruction and curve reconstruction. Two actual range images, "jumble2" and "foot2" from the MSU PRIP Lab are shown in Figure 7.6 and 7.7, respectively. They have flat and curved surfaces. To test for invariance, we use DATAl in Figure 7.3 and DATA2 in Figure 7.4. These two images have two inclined planes of which the slopes are $\tan 15^\circ$ and $\tan 75^\circ$. DATA2 in Figure 7.4 is obtained by rotating DATAl in Figure 7.3 by 60 degree about the y-axis. Figure 7.5 shows a section of DATAl and DATA2 after $N(0,1)$ is added in the direction of the surface normal vector. In order to show the invariance property, dense and sparse DATAl and DATA2 that are noisy are reconstructed and the reconstructed result for DATA2 is rotated back into correspondence with DATAl. The difference between the two reconstructed surfaces is examined by computing the volume between them divided by the average surface area of the two reconstructions. Similarly an invariance test on curve reconstruction is carried out for two corresponding slices of DATA1 and DATA2. The reconstruction result of the slice of DATA2 is rotated back and the difference between the two reconstructed curves is compared by computing the area between them divided by the average arc length of the two reconstructions.

Synthetic noisy range images are generated by the equation,

$$\begin{aligned} z'(x,y) &= z(x,y) + N(0,\sigma^2)\sec\phi \\ &= z(x,y) + N(0,\sigma^2)\sqrt{1+z_x^2+z_y^2} \end{aligned} \tag{7.1}$$

where $N(0,\sigma^2)$ represents Gaussian noise with mean 0 and standard deviation σ and $z(x,$ y) and $z'(x,y)$ denotes noiseless and noisy images respectively. sec 4, which is the inverse of the surface slant cos ϕ, is multiplied to $N(0,\sigma^2)$ in order to add noise in the direction of the surface normal vector, which is in agreement with our assumption about noise described in an earlier section of the paper. The effect is that more noise is added to regions with high slope. Sparse noisy images (or curves) are generated by randomly deleting pixels of a noisy image (or curve). For clear visual comparison of reconstruction results, a section of the reconstruction results are displayed for the original noiseless data, IDFIT-BIASED, and IDFIT-UNBIASED methods. FIT is not shown on these plots because the performance of FIT is always worse than the other two methods. The performance of FIT compared to the other two methods is shown in Figures 7.16, 7.17 for surface reconstruction and Figures 7.25, 7.26 for curve reconstruction. The tables (Table 7.1 and Table 7.2) also show a comparison of all three algorithms based on our performance measures V/A and A/L.

7.1 surface-reconstruction

The reconstruction results of the curved-inclined image for IDFIT-BIASED and IDFIT-UNBIASED are shown in the case of a dense image in Figures 7.8, 7.9 and a sparse image in Figures 7.10, 7.11 where 80% of the pixels are missing. For both cases, IDFIT-UNBIASED better preserves discontinuities than IDFIT-BIASED and is capable of reconstruction of inclined and curved surfaces although it is a first order model. The reconstruction results when $\lambda = 30.0$ indicate the robustness property of IDFIT-UNBIASED to the smoothing parameter λ. IDFIT-BIASED results in more and more blurring as λ gets large in contrast to the performance of IDFIT-UNBIASED whose performance does not appreciably degrade. Figures

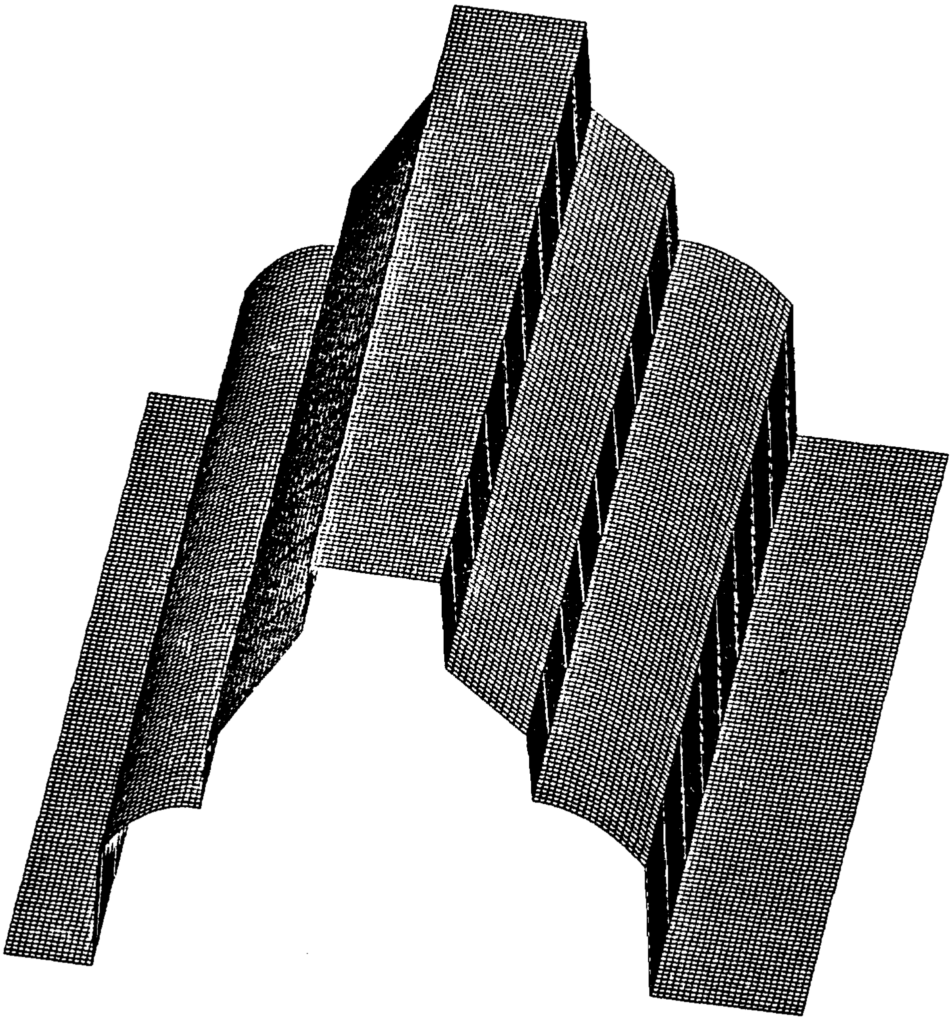

Figure 7.1: Three-dimensional display of curved-inclined image

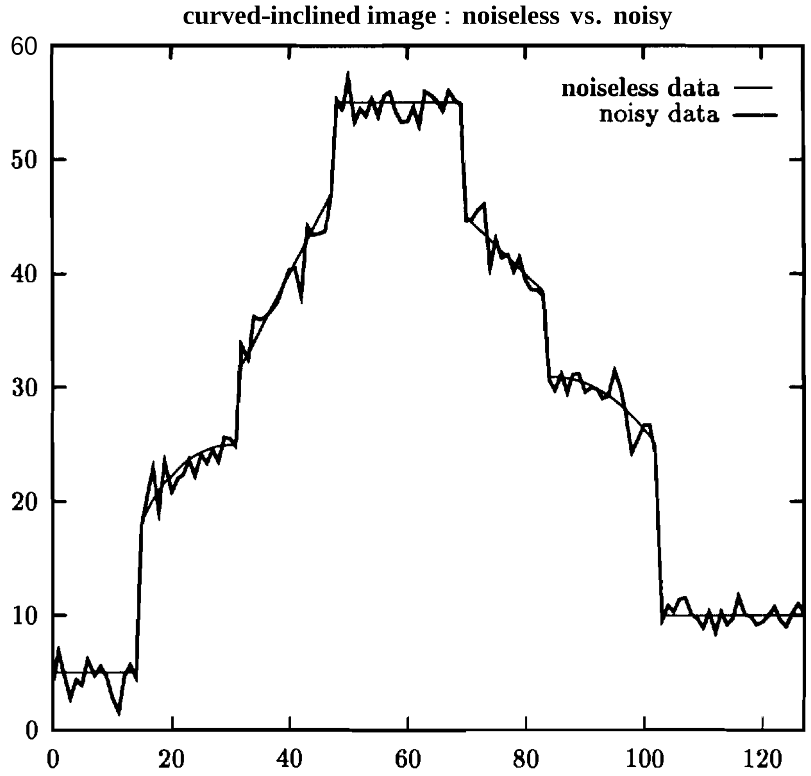

Figure 7.2: A section of curved-inclined image: noiseless vs. noisy. $N(0,1)$ is added in the direction of surface normal vector.

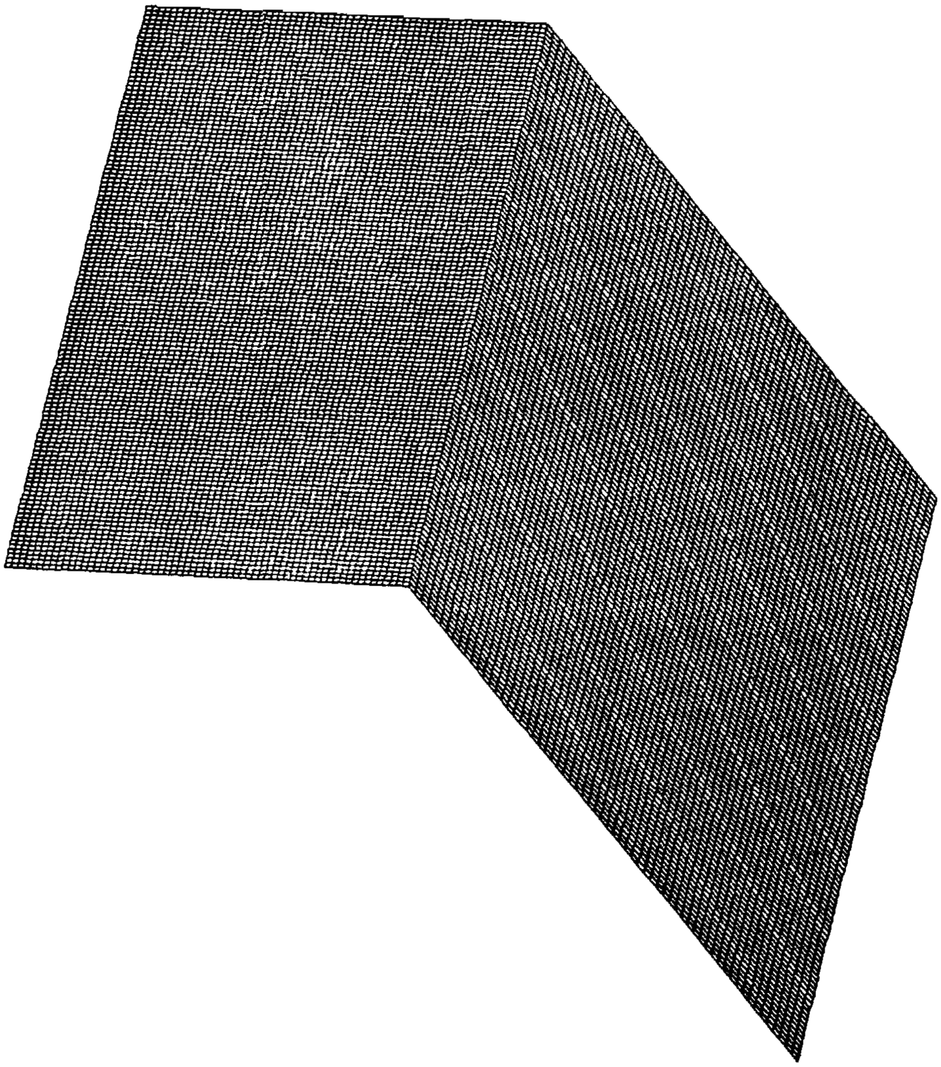

Figure 7.3: Three-dimensional display of invariance test data, DATA1

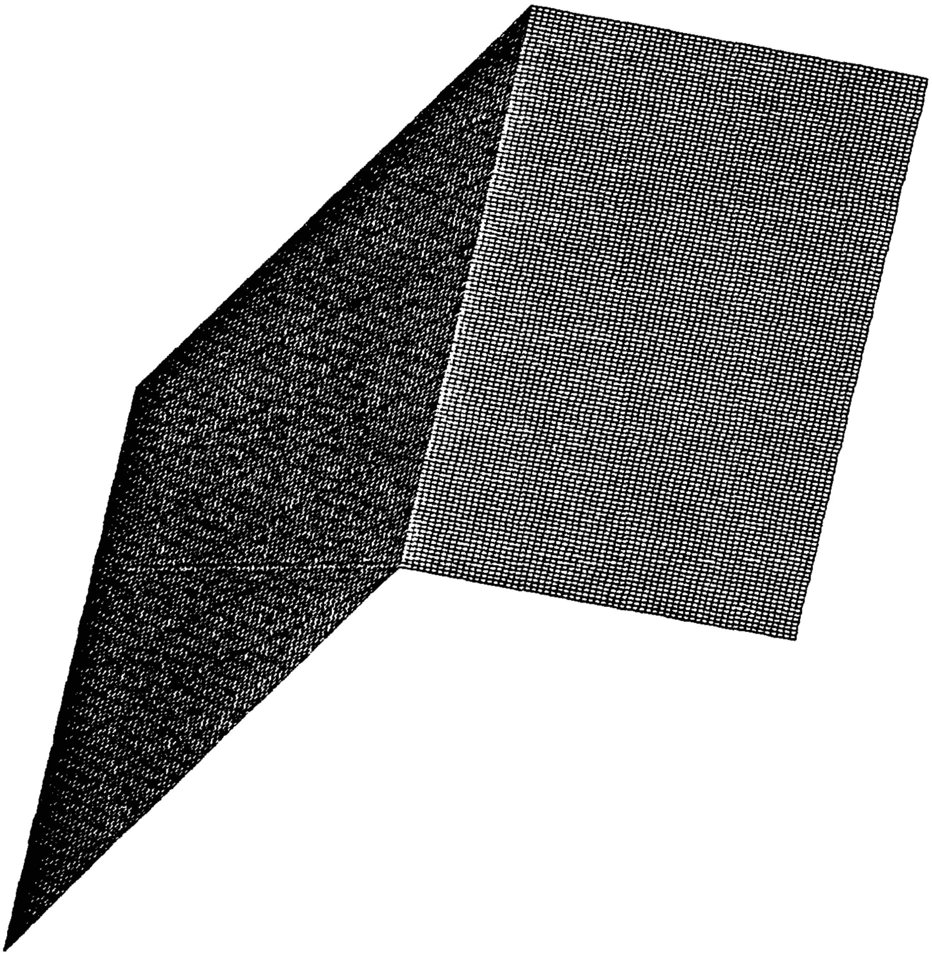

Figure 7.4: Three-dimensional display of invariance test data, DATA2

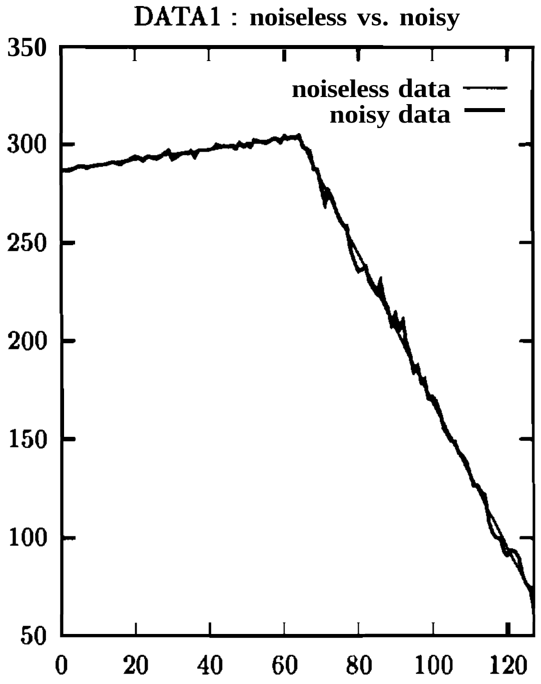

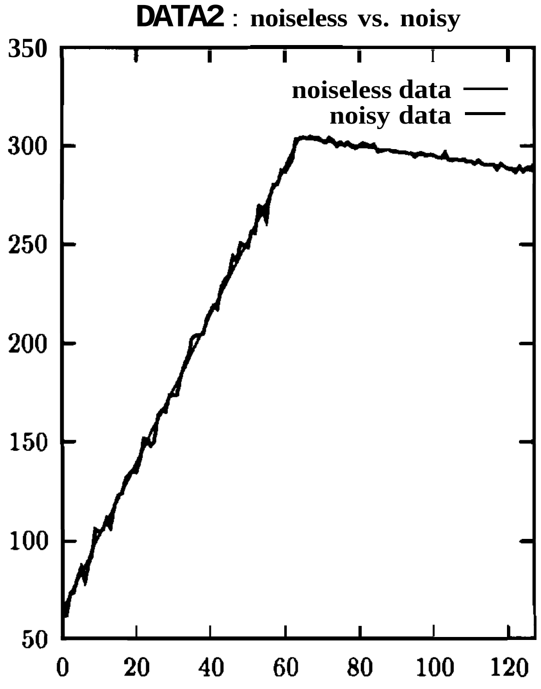

Figure 7.5: A section display of DATA1 and DATA2: noiseless vs. noisy. $N(0,1)$ is added in the direction of surface normal vector.

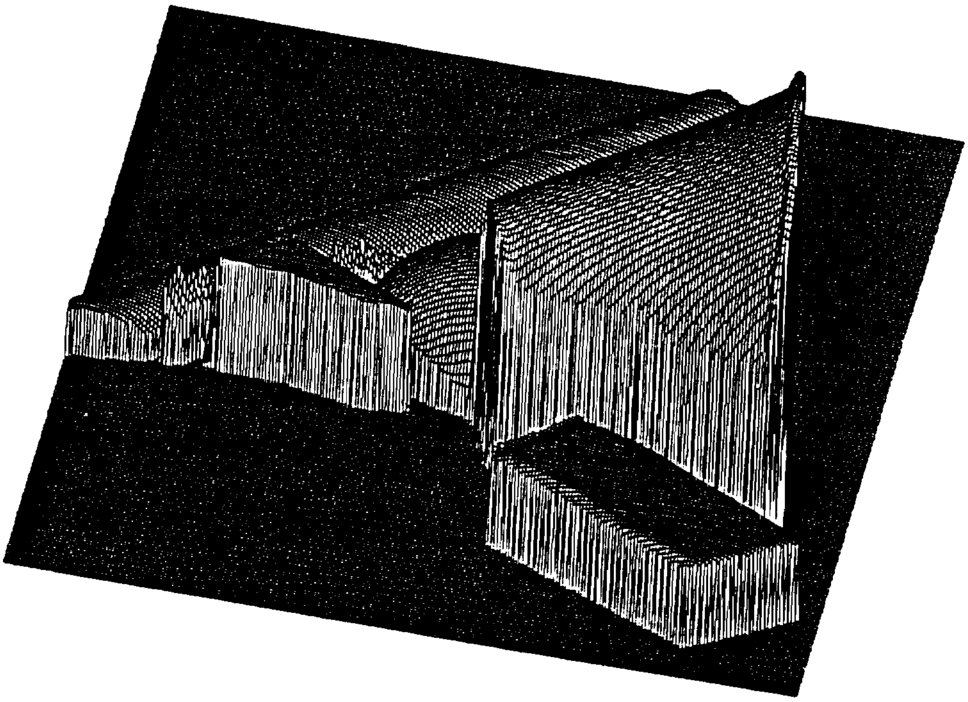

Figure 7.6: Three-dimensional display of “jumble2”

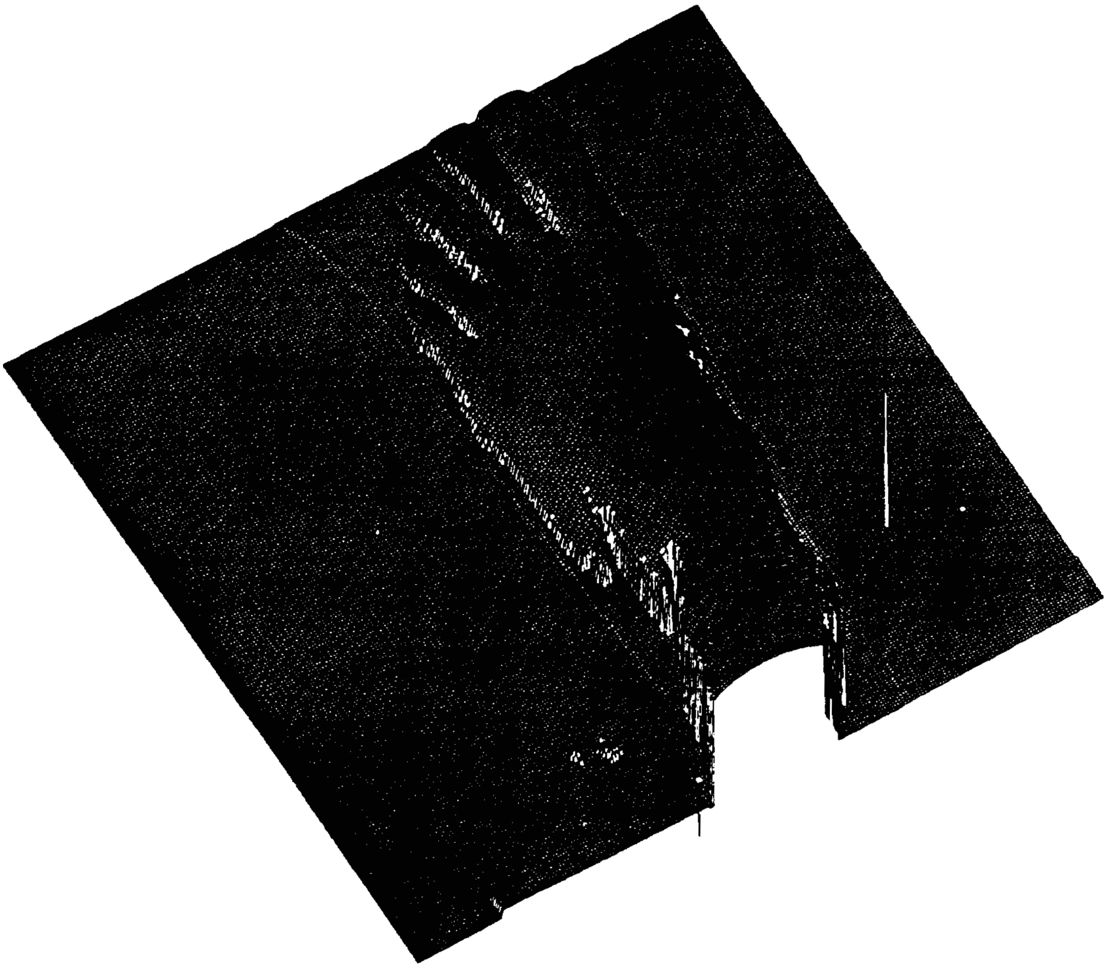

Figure 7.7: Three-dimensional display of “foot2”

7.16 and 7.17 show the performance measure (V/A) for FIT, IDFIT-BIASED, and IDFIT-UNBIASED for $\lambda(0.0 \sim 5.0)$ and $\lambda(0.0 \sim 30.0)$, respectively. The robustness property of IDFIT-UNBIASED is clearly demonstrated for a wide range of λ. The data (V/A) plotted in Figure 7.17 is listed in Table 7.1. Figures 7.12 and 7.13 illustrate the results of invariance tests for one slice of the image. The invariance performance of IDFIT-UNBIASED and IDFIT-BIASED is not much different from each other. On the other hand, FIT performs worse than IDFIT-UNBIASED and IDFIT-BIASED with respect to invariance. When the data is dense, the reconstructed surface follows the data closely for all three reconstructions as shown in Figure 7.12. See V/A values in Figure 7.12. However, the difference in the invariance property between FIT and IDFIT-UNBIASED and IDFIT-BIASED is still visible. As the sparseness of input image increases (i.e. when there are fewer data points), the invariance performance of FIT gets much worse than that of IDFIT-UNBIASED and IDFIT-BIASED. See Figure 7.13 where 90% of the pixels are missing. Invariance of IDFIT-UNBIASED ($V/A = 0.2971$) and IDFIT-BIASED ($V/A = 0.3340$) is much better than FIT ($V/A = 0.7070$). Figures 7.14 and 7.15 show the reconstruction results of the actual images “jumble2” and “foot2”, respectively. They clearly show that IDFIT-UNBIASED performs better that IDFIT-BIASED in preservation of discontinuities. The value of V/A measure for FIT in the case of “jumble2” is 0.0658 and 0.1201 in the case of “foot2” although the sections of the reconstructed surface are not displayed in Figures 7.14 and 7.15.

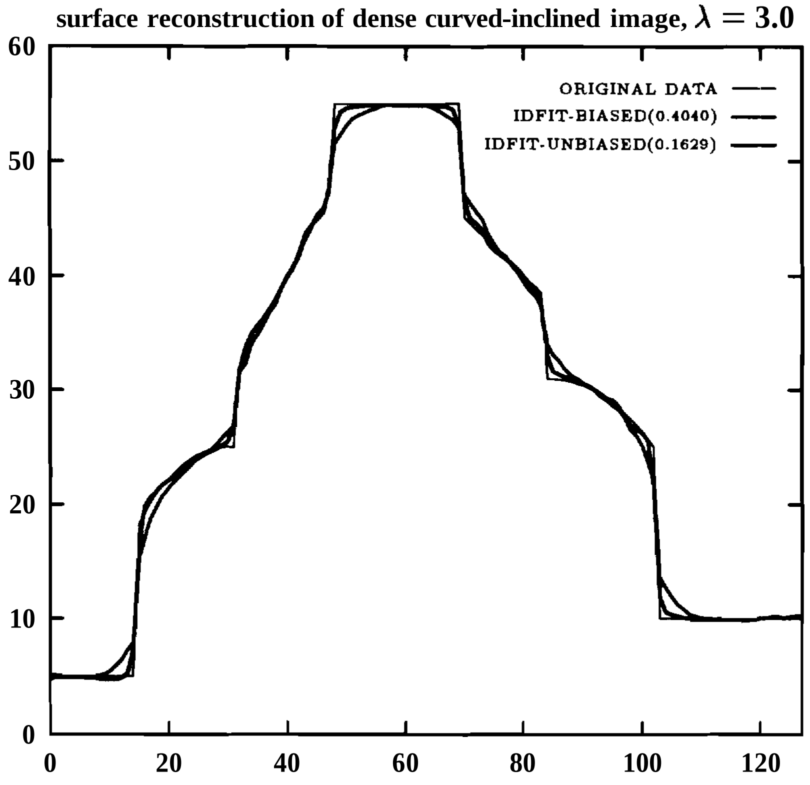

Figure 7.8: Surface reconstruction of dense curved-inclined image for $\lambda = 3.0$.

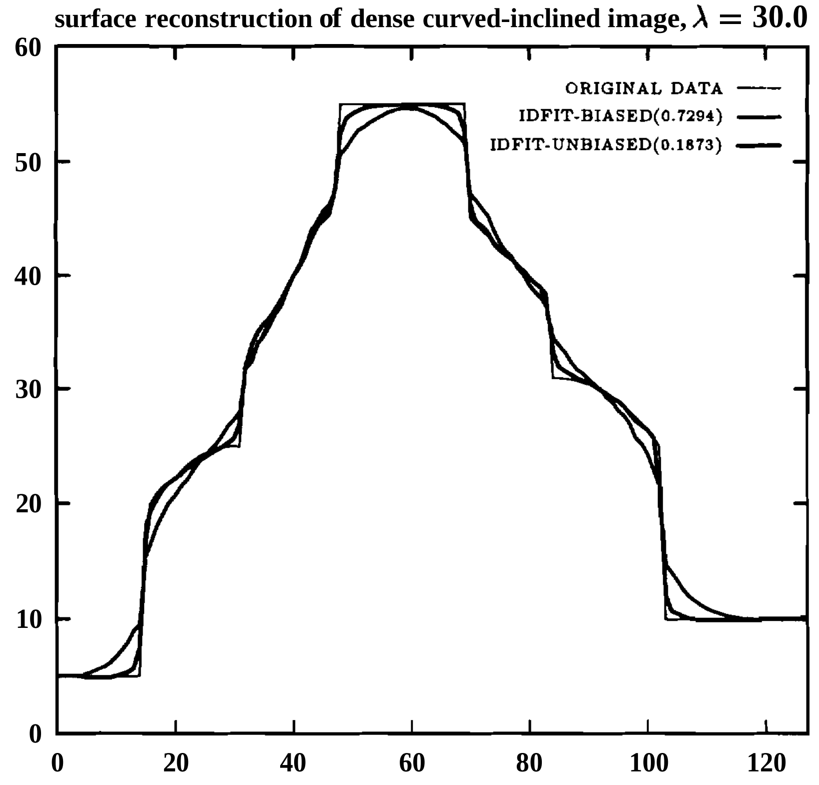

Figure 7.9: Surface reconstruction of dense curved-inclined image for A = 30.0.

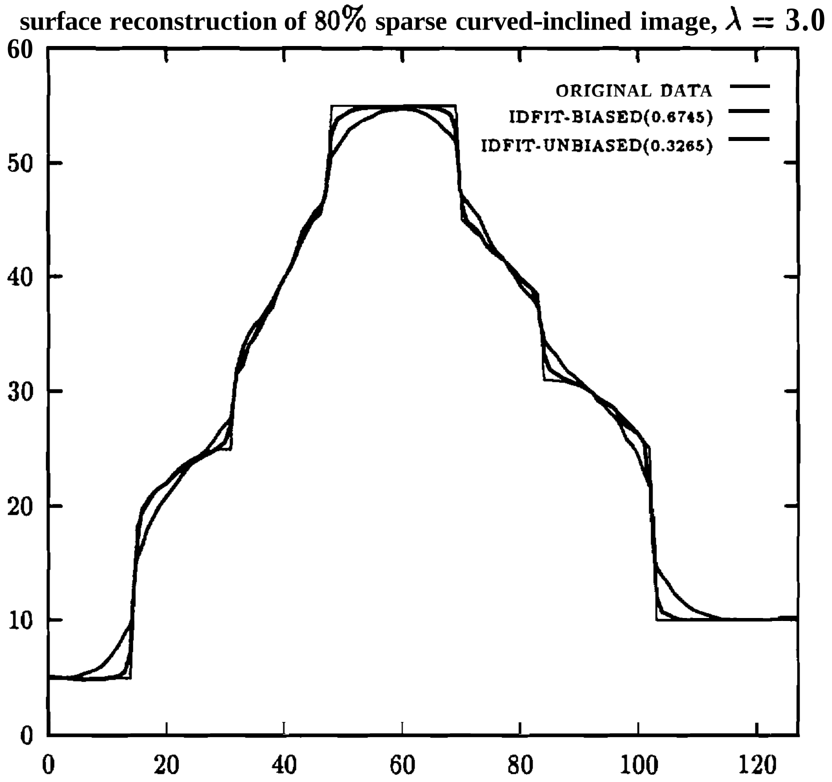

Figure 7.10: Surface reconstruction of 80% sparse curved-inclined image for $\lambda = 3.0$.

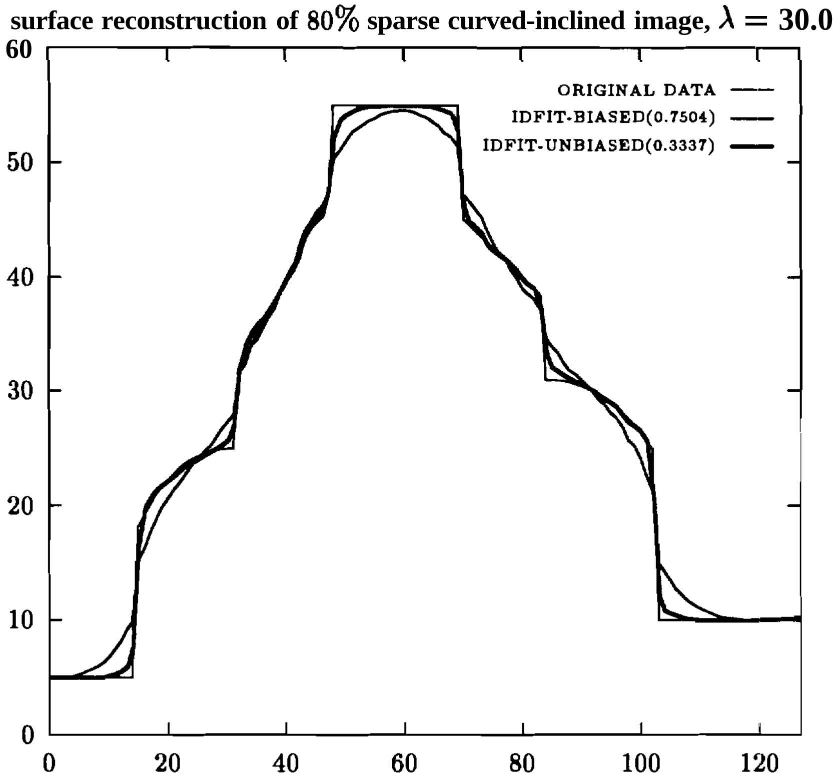

Figure 7.11: Surface reconstruction of 80% sparse curved-inclined image for $\lambda = 30.0$.

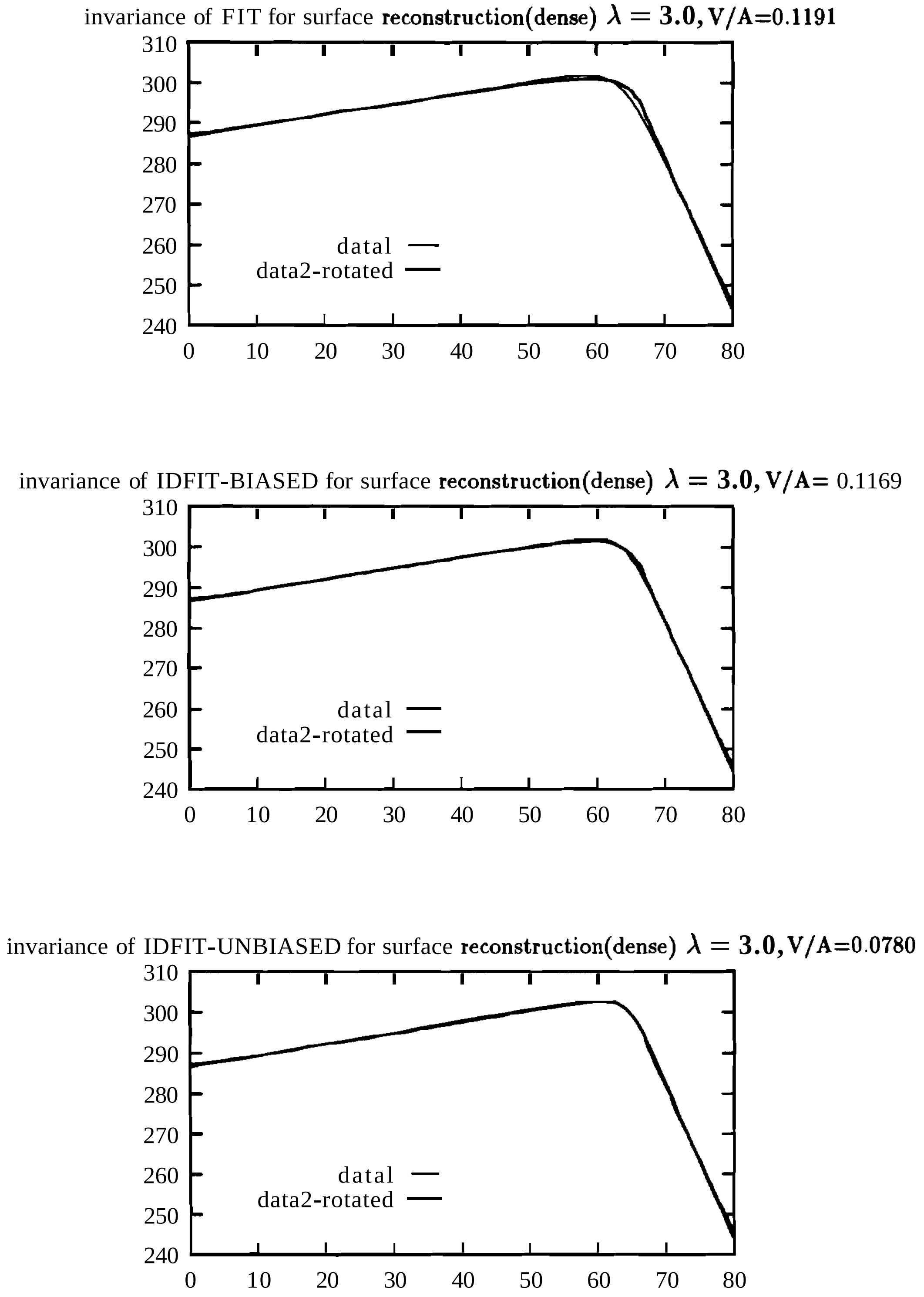

invariance of FIT for surface reconstruction(dense) $\lambda = 3.0$, V/A=0.1191

invariance of IDFIT-BIASED for surface reconstruction(dense) $\lambda = 3.0$, V/A= 0.1169

invariance of IDFIT-UNBIASED for surface reconstruction(dense) $\lambda = 3.0$, V/A=0.0780

Figure 7.12: Invariance performance of FIT, IDFIT-BIASED, and IDFIT-UNBIASED for dense surface

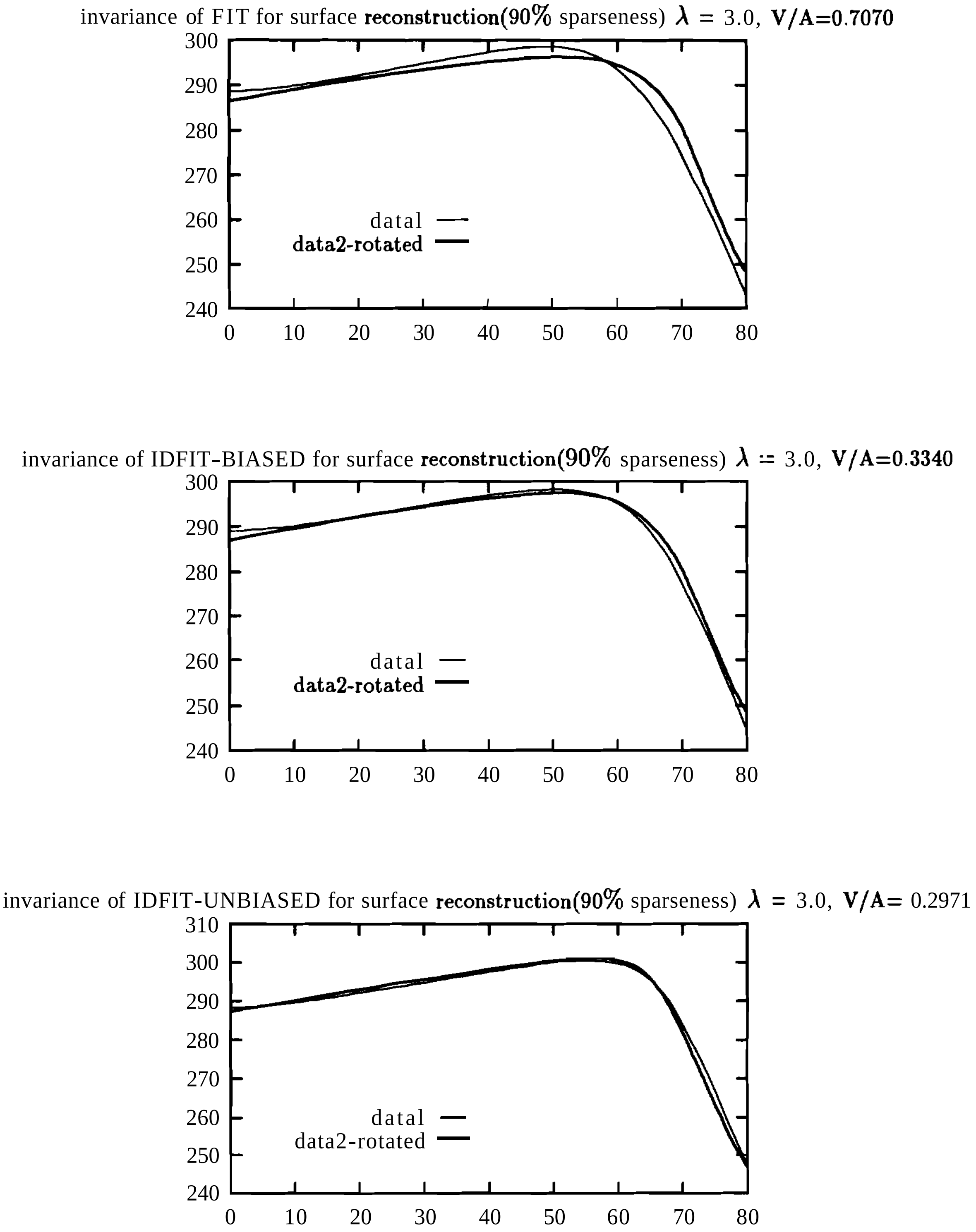

invariance of FIT for surface reconstruction(90% sparseness) λ = 3.0, V/A=0.7070

invariance of IDFIT-BIASED for surface reconstruction(90% sparseness) λ = 3.0, V/A=0.3340

invariance of IDFIT-UNBIASED for surface reconstruction(90% sparseness) λ = 3.0, V/A= 0.2971

Figure 7.13: Invariance performance of FIT, IDFIT-BIASED, and IDFIT-UNBIASED for 90% sparse surface

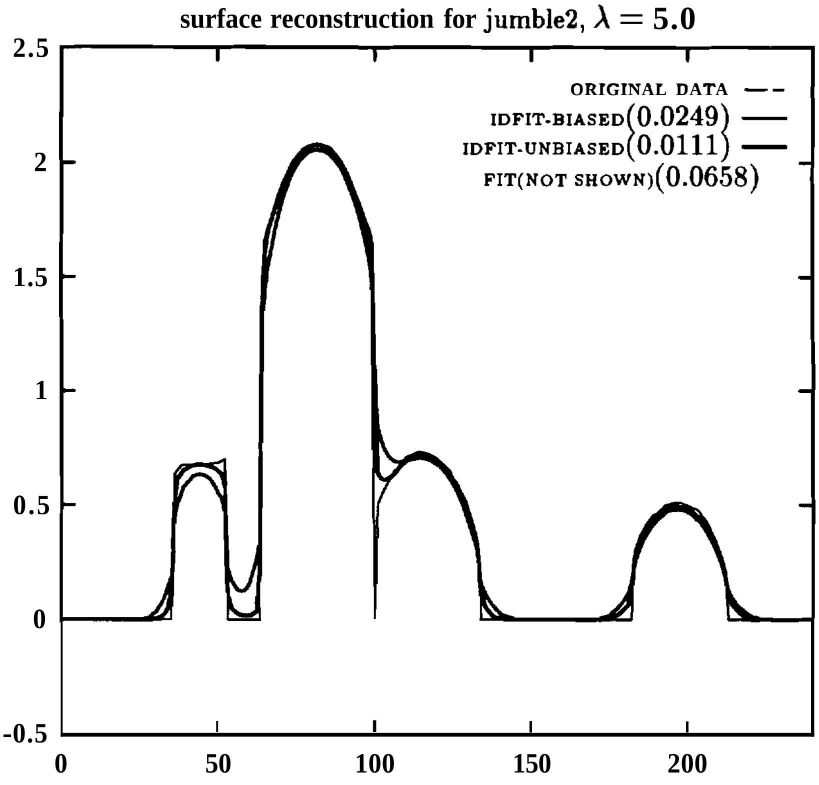

Figure 7.14: Surface reconstruction of "jumble2" (dense) for $\lambda = 5.0$.

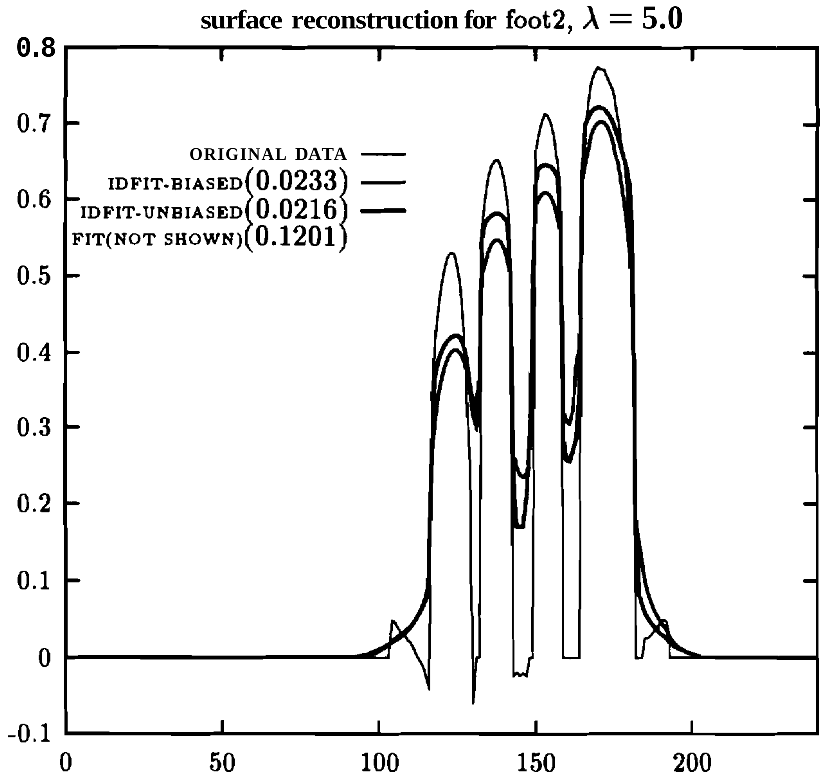

Figure 7.15: Surface reconstruction of "foot2" (dense) for $\lambda = 5.0$.

λ	dense			sparseness 50%			sparseness 80%		
	FIT	IDFIT-BIASED	IDFIT-UNBIASED	FIT	IDFIT-BIASED	IDFIT-UNBIASED	FIT	IDFIT-BIASED	IDFIT-UNBIASED
0.0	0.2831	0.2831	0.2831	0.3448	0.3247	0.3328	0.4781	0.4310	0.4142
1.0	0.2735	0.2151	0.1858	0.4171	0.3320	0.2320	0.6314	0.5145	0.3376
2.0	0.4676	0.3049	0.1620	0.6682	0.4341	0.2135	0.8583	0.6253	0.3268
3.0	0.6582	0.4040	0.1629	0.8369	0.5076	0.2201	0.9808	0.6745	0.3265
4.0	0.8077	0.4829	0.1684	0.9598	0.5530	0.2246	1.0520	0.7077	0.3312
5.0	0.9197	0.5414	0.1698	1.0268	0.5880	0.2259	1.0949	0.7156	0.3319
6.0	1.0119	0.5819	0.1765	1.0768	0.6176	0.2300	1.1186	0.7298	0.3324
7.0	1.0805	0.6164	0.1775	1.1173	0.6343	0.2306	1.1375	0.7326	0.3327
8.0	1.1297	0.6374	0.1781	1.1417	0.6490	0.2310	1.1432	0.7345	0.3329
9.0	1.1721	0.6555	0.1785	1.1519	0.6526	0.2313	1.1576	0.7359	0.3331
10.0	1.1994	0.6617	0.1822	1.1698	0.6650	0.2315	1.1606	0.7368	0.3332
11.0	1.2231	0.6766	0.1825	1.1860	0.6670	0.2317	1.1628	0.7375	0.3333
12.0	1.2442	0.6803	0.1827	1.1905	0.6785	0.2318	1.1645	0.7479	0.3334
13.0	1.2633	0.6936	0.1828	1.1940	0.6797	0.2319	1.1658	0.7483	0.3334
14.0	1.2702	0.6960	0.1830	1.2074	0.6807	0.2320	1.1773	0.7487	0.3335
15.0	1.2867	0.7083	0.1831	1.2097	0.6815	0.2321	1.1781	0.7490	0.3335
16.0	1.3022	0.7100	0.1832	1.2116	0.6822	0.2321	1.1789	0.7492	0.3335
17.0	1.3063	0.7114	0.1833	1.2132	0.6828	0.2322	1.1794	0.7494	0.3336
18.0	1.3098	0.7125	0.1833	1.2146	0.6832	0.2322	1.1799	0.7496	0.3336
19.0	1.3235	0.7135	0.1834	1.2157	0.6836	0.2322	1.1804	0.7497	0.3336
20.0	1.3261	0.7248	0.1870	1.2167	0.6939	0.2323	1.1807	0.7498	0.3336
21.0	1.3283	0.7255	0.1870	1.2175	0.6942	0.2323	1.1810	0.7499	0.3336
22.0	1.3410	0.7262	0.1871	1.2289	0.6945	0.2359	1.1813	0.7500	0.3336
23.0	1.3428	0.7268	0.1871	1.2296	0.6947	0.2359	1.1815	0.7501	0.3336
24.0	1.3443	0.7273	0.1871	1.2301	0.6949	0.2359	1.1817	0.7501	0.3336
25.0	1.3457	0.7277	0.1872	1.2306	0.6951	0.2359	1.1819	0.7502	0.3336
26.0	1.3469	0.7281	0.1872	1.2311	0.6952	0.2360	1.1821	0.7503	0.3337
27.0	1.3479	0.7285	0.1872	1.2315	0.6954	0.2360	1.1822	0.7503	0.3337
28.0	1.3489	0.7288	0.1872	1.2318	0.6955	0.2360	1.1823	0.7503	0.3337
29.0	1.3606	0.7291	0.1873	1.2322	0.6956	0.2360	1.1825	0.7504	0.3337
30.0	1.3614	0.7294	0.1873	1.2324	0.6957	0.2360	1.1826	0.7504	0.3337

Table 7.1: V/A measure for surface reconstruction of the curved-inclined image for various λ

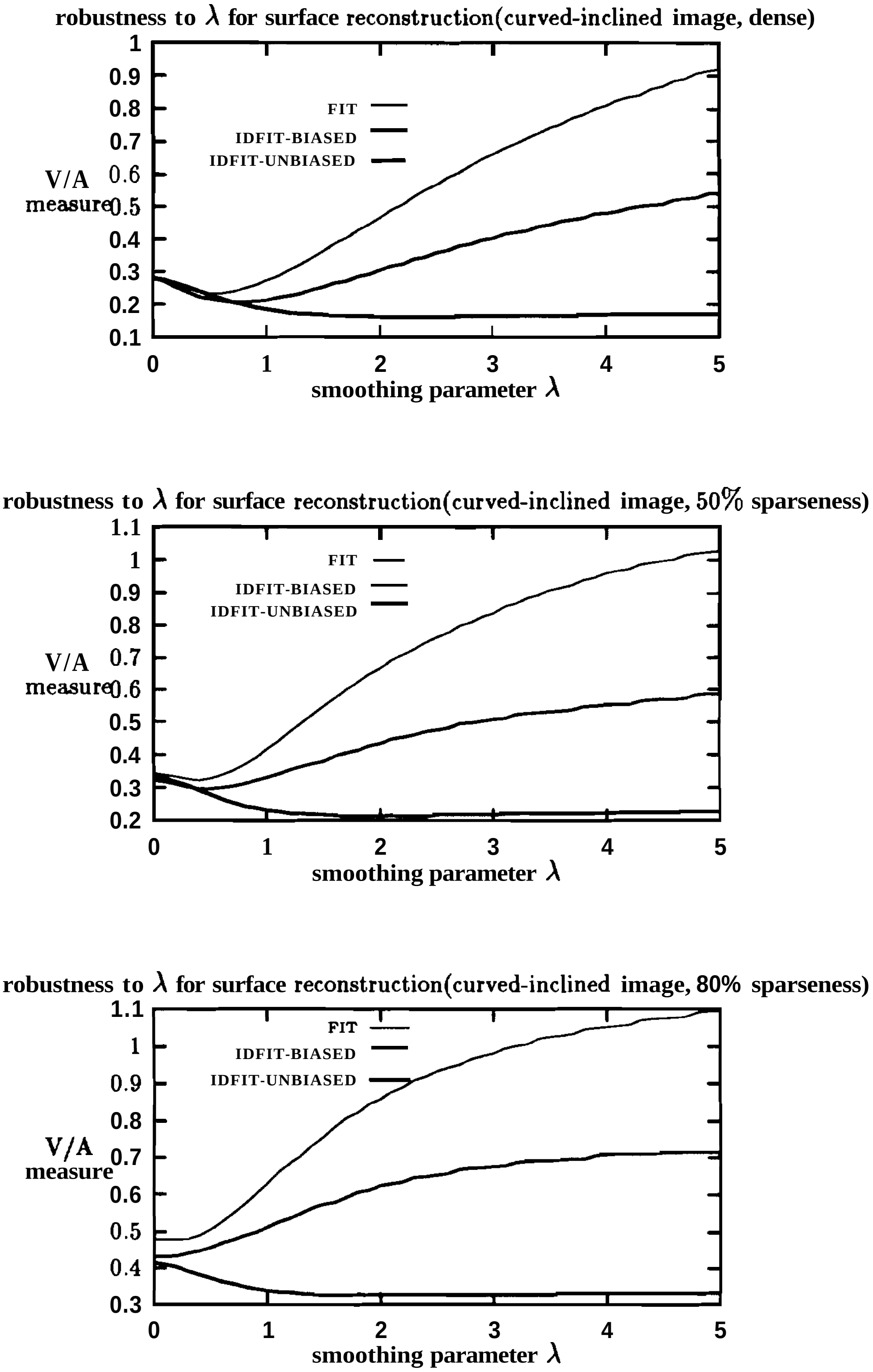

robustness to λ for surface reconstruction(curved-inclined image, dense)

robustness to λ for surface reconstruction(curved-inclined image, 50% sparseness)

robustness to λ for surface reconstruction(curved-inclined image, 80% sparseness)

Figure 7.16: Robustness of surface reconstruction to X

7.2 curve-reconstruction

Slices of images used for surface reconstruction are adopted as input data for curve reconstruction. Results similar to those in surface reconstruction are obtained for curve reconstruction. However, curve reconstruction turns out to be harder than surface reconstruction for the data of the same percentage sparseness because one dimensional data of the same percentage sparseness has fewer neighbors with data than two dimensional sparse data, and so there are fewer constraints for reconstruction. Figures 7.18-7.21 show the reconstruction results of a section of the noisy curved-inclined image. IDFIT-UNBIASED better preserves discontinuities than IDFIT-BIASED and is capable of reconstruction of inclined and curved surfaces although it is a first order model. In Figures 7.25 and 7.26, the robustness property of IDFIT-UNBIASED to the smoothing parameter λ is shown for curve reconstruction. While IDFIT-BIASED results in more and more blurring as λ gets large, the performance of IDFIT-UNBIASED does not appreciably degrade. The plot data (A/L) for Figure 7.26 is listed in Table 7.2. Figures 7.22 and 7.23 illustrate the results of invariance tests for curve reconstruction. When the data is dense, the reconstructed surface follows the data closely for all three reconstructions as shown in Figure 7.22. However, the difference in the invariance property is still visible. For a sparse image of which 80% of the pixels are missing, the performance with respect to invariance of IDFIT-UNBIASED $(A/L = 0.7921)$ is much better than that of IDFIT-BIASED $(A/L =$ 1.0931) and FIT $(A/L = 1.4286)$. Figure 7.24 shows the reconstruction results of a slice taken from the actual range image "jumble2". It clearly shows that IDFIT-UNBIASED performs better that IDFIT-BIASED in preservation of discontinuities. The value of A/L measure for FIT is 0.0917 although the reconstructed curve is not displayed in Figure 7.24.

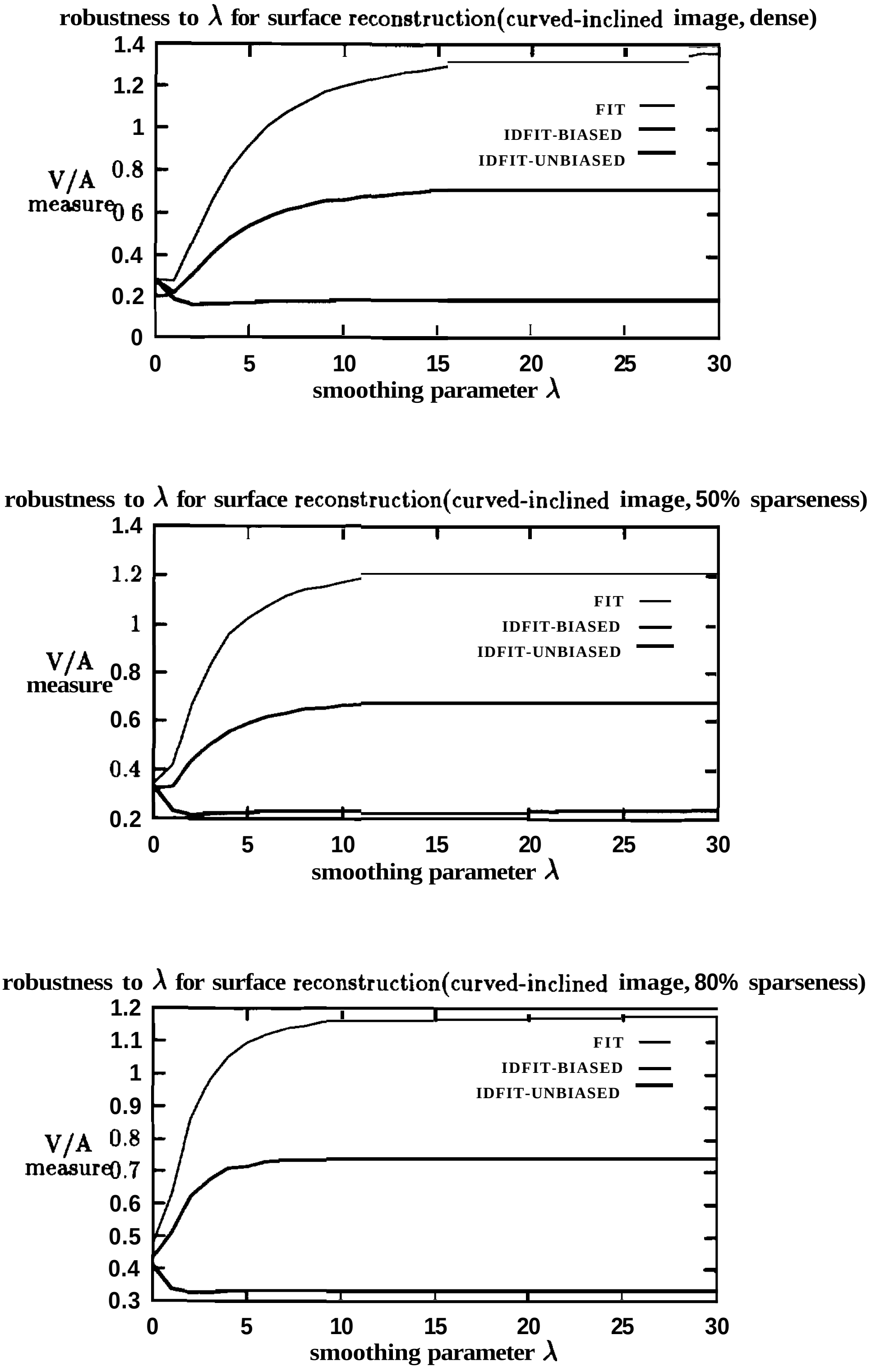

Figure 7.17: Robustness of surface reconstruction to X

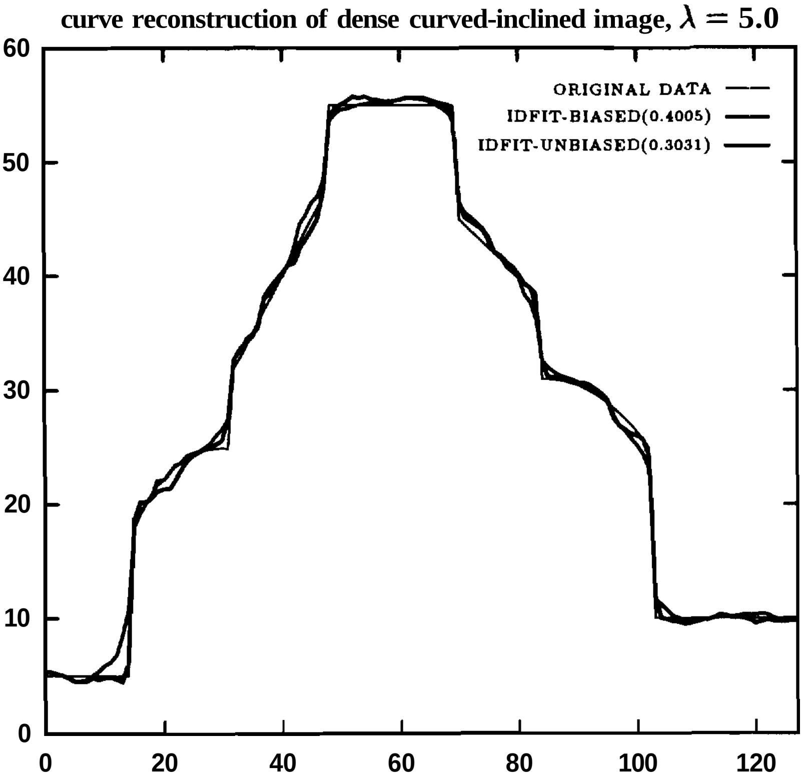

Figure 7.18: Curve reconstruction of a slice of dense curved-inclined image for $\lambda = 5.0$.

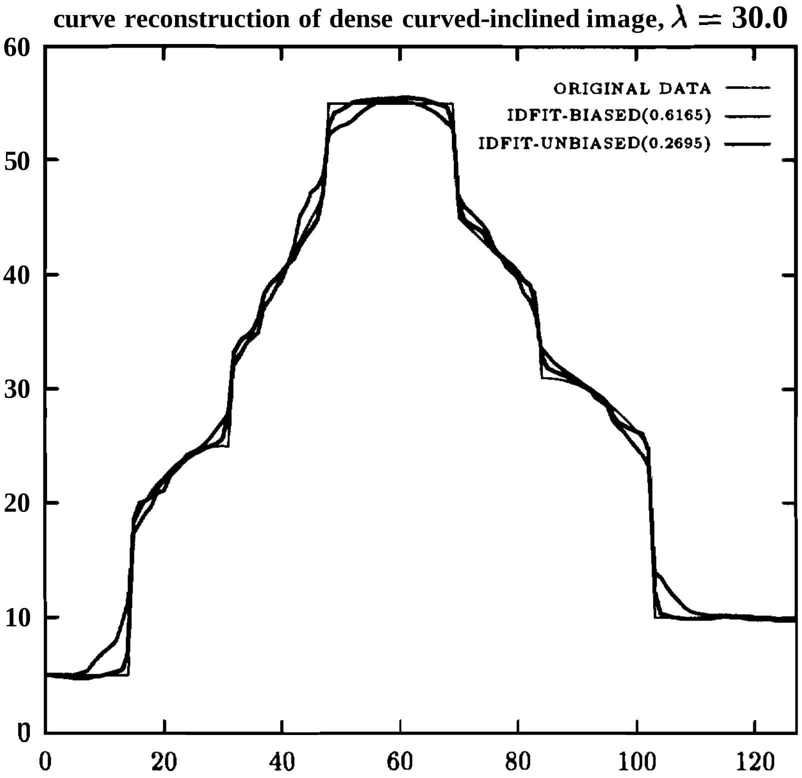

Figure 7.19: Curve reconstruction of a slice of dense curved-inclined image for $\lambda = 30.0$.

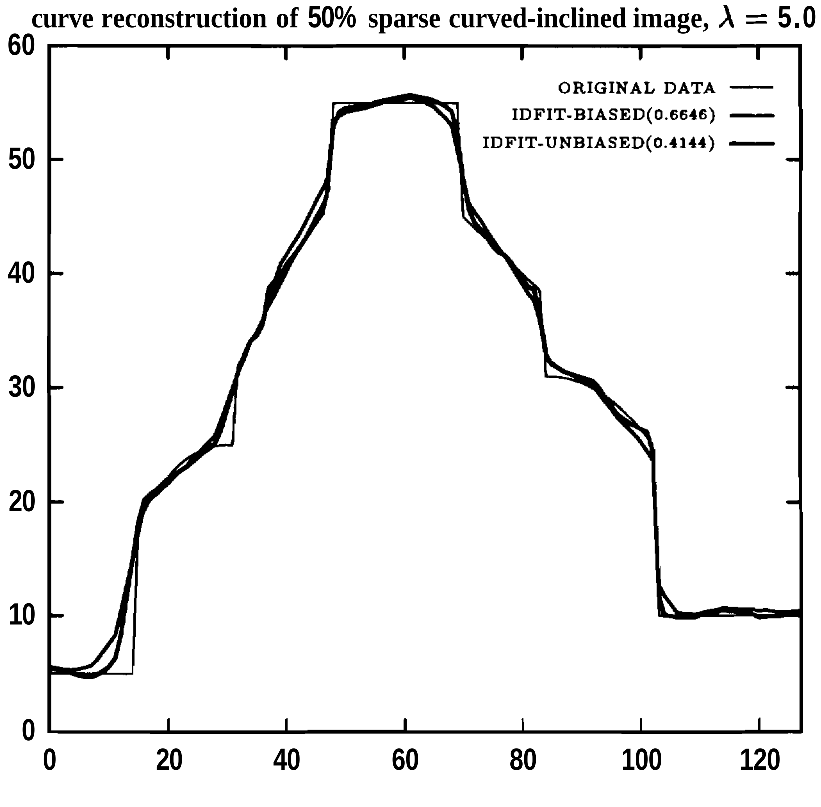

Figure 7.20: Curve reconstruction of a slice of 50% sparse curved-inclined image for $\lambda = 5.0$.

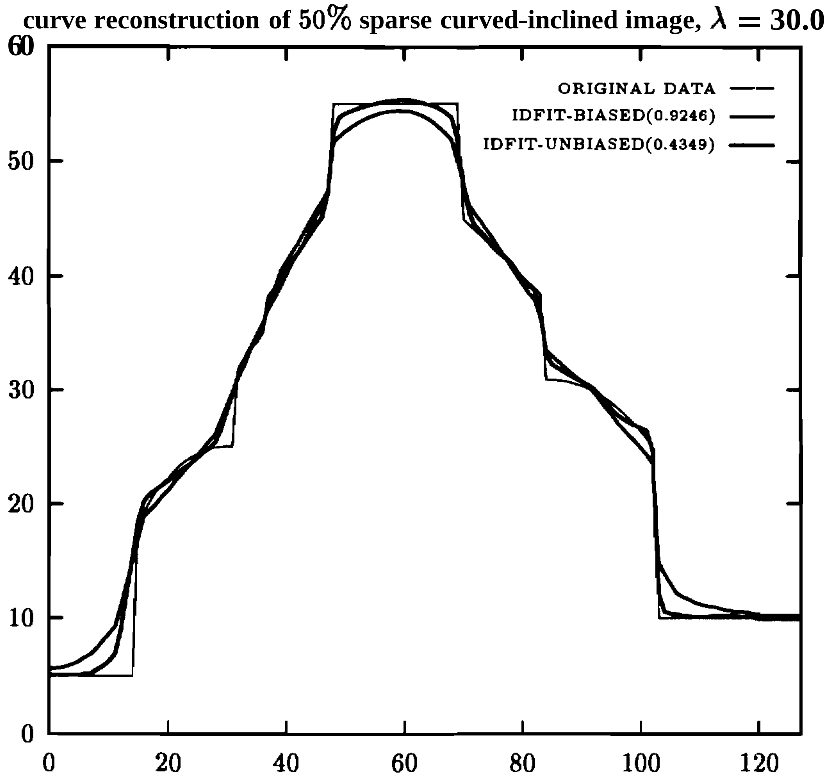

Figure 7.21: Curve reconstruction of a slice of 50% sparse curved-inclined image for $\lambda = 30.0$.

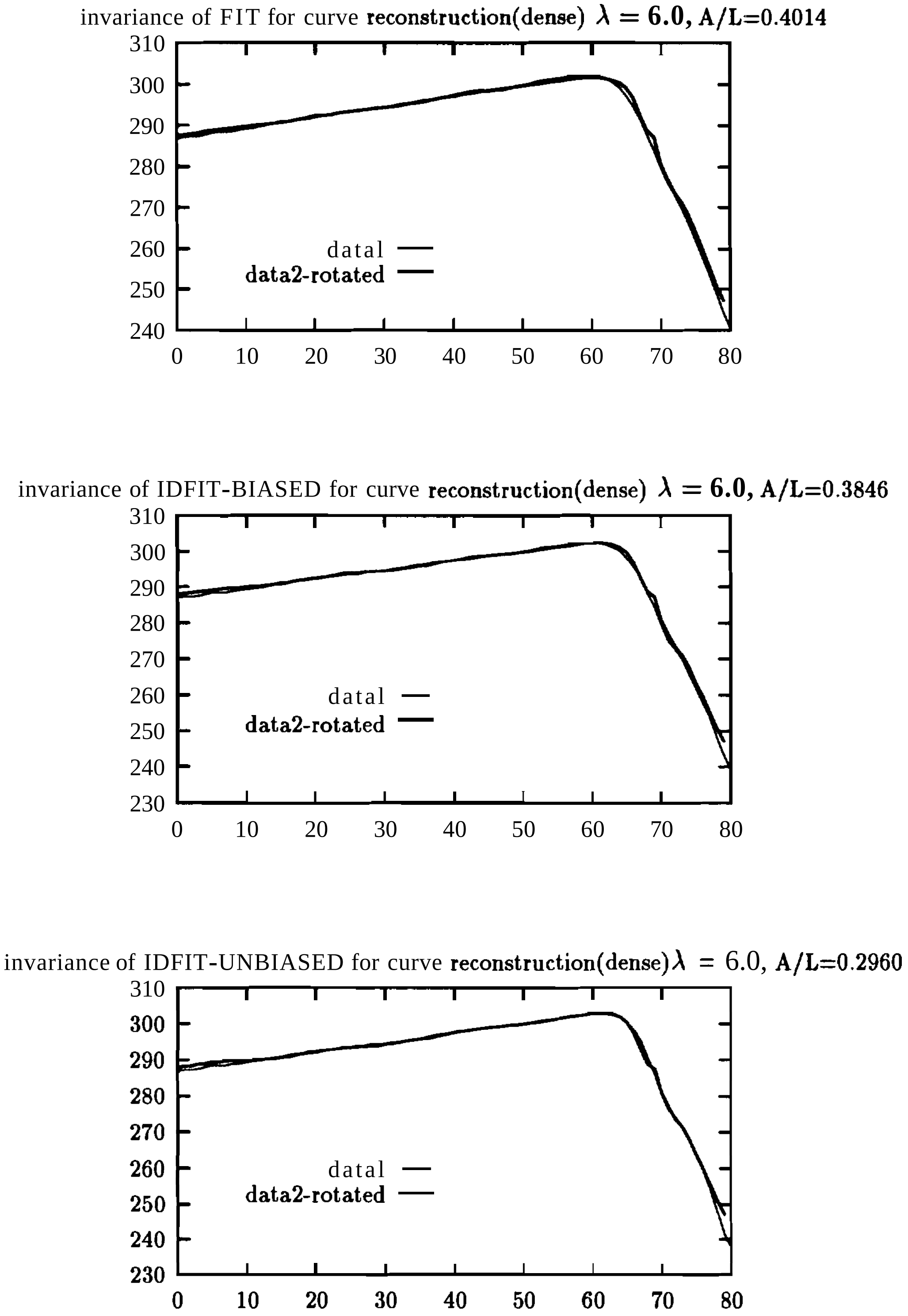

invariance of FIT for curve reconstruction(dense) $\lambda = 6.0$, A/L=0.4014

invariance of IDFIT-BIASED for curve reconstruction(dense) $\lambda = 6.0$, A/L=0.3846

invariance of IDFIT-UNBIASED for curve reconstruction(dense)λ = 6.0, A/L=0.2960

Figure 7.22: Invariance performance of FIT, IDFIT-BIASED, and IDFIT-UNBIASED for dense curve

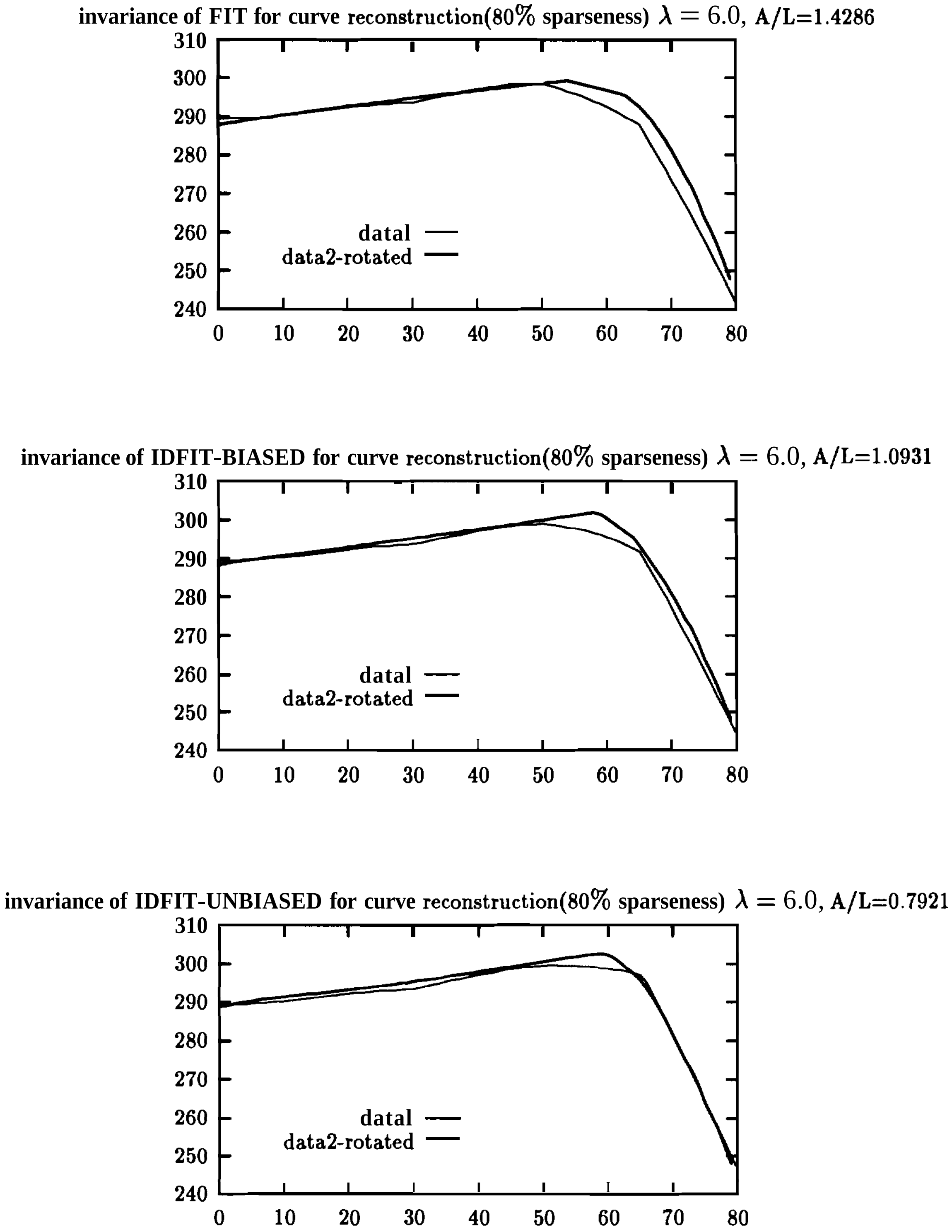

invariance of FIT for curve reconstruction(80% sparseness) $\lambda = 6.0$, A/L=1.4286

invariance of IDFIT-BIASED for curve reconstruction(80% sparseness) $\lambda = 6.0$, A/L=1.0931

invariance of IDFIT-UNBIASED for curve reconstruction(80% sparseness) $\lambda = 6.0$, A/L=0.7921

Figure 7.23: Invariance performance of FIT, IDFIT-BIASED, and IDFIT-UNBIASED for 80% sparse curve

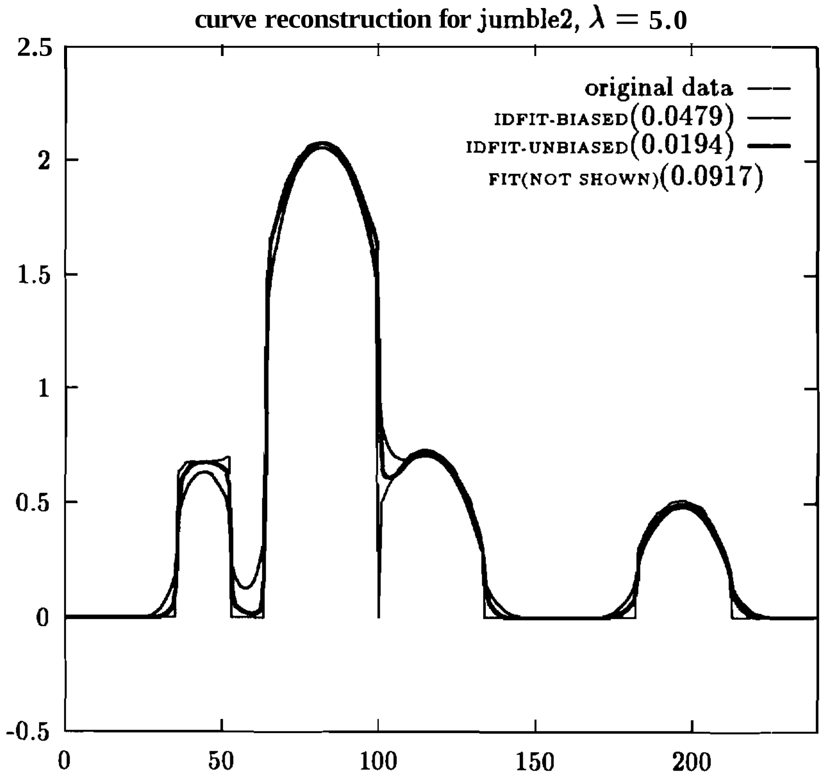

Figure 7.24: Curve reconstruction of a slice of "jumble2" (dense) for $\lambda = 5.0$.

λ	dense			sparseness 50%			sparseness 80%		
	FIT	IDFIT-BIASED	IDFIT-UNBIASED	FIT	IDFIT-BIASED	IDFIT-UNBIASED	FIT	IDFIT-BIASED	IDFIT-UNBIASED
0.0	0.4917	0.4917	0.4917	0.5745	0.5718	0.5703	1.3555	1.3125	1.2892
1.0	0.4179	0.3797	0.3561	0.6439	0.5762	0.4495	1.2910	1.1732	1.1492
2.0	0.4833	0.3813	0.3353	0.7413	0.5942	0.4306	1.2881	1.0856	1.0633
3.0	0.5377	0.3836	0.3215	0.8271	0.6170	0.4218	1.2764	1.0416	1.0167
4.0	0.5828	0.3898	0.3112	0.8965	0.6430	0.4170	1.2600	1.0220	0.9790
5.0	0.6216	0.4005	0.3031	0.9546	0.6646	0.4144	1.2514	1.0306	0.9520
6.0	0.6574	0.4134	0.2963	1.0006	0.6892	0.4116	1.2536	1.0407	0.9272
7.0	0.6913	0.4216	0.2910	1.0411	0.7079	0.4117	1.2726	1.0545	0.9225
8.0	0.7224	0.4349	0.2864	1.0780	0.7206	0.4104	1.3113	1.0711	0.9199
9.0	0.7517	0.4427	0.2827	1.1130	0.7377	0.4119	1.3371	1.0886	0.9184
10.0	0.7754	0.4566	0.2793	1.1455	0.7547	0.4116	1.3614	1.0954	0.9273
11.0	0.8011	0.4704	0.2767	1.1755	0.7656	0.4144	1.3844	1.1117	0.9274
12.0	0.8256	0.4780	0.2745	1.2035	0.7825	0.4149	1.4271	1.1173	0.9278
13.0	0.8447	0.4920	0.2729	1.2297	0.7987	0.4155	1.4579	1.1328	0.9283
14.0	0.8679	0.4987	0.2718	1.2470	0.8073	0.4197	1.4877	1.1375	0.9390
15.0	0.8903	0.5120	0.2710	1.2703	0.8150	0.4203	1.5164	1.1524	0.9397
16.0	0.9060	0.5180	0.2704	1.2926	0.8295	0.4209	1.5443	1.1671	0.9403
17.0	0.9269	0.5307	0.2699	1.3061	0.8362	0.4215	1.5625	1.1709	0.9410
18.0	0.9408	0.5361	0.2695	1.3266	0.8499	0.4221	1.5891	1.1852	0.9416
19.0	0.9607	0.5486	0.2692	1.3382	0.8557	0.4263	1.6063	1.1885	0.9526
20.0	0.9733	0.5536	0.2692	1.3573	0.8610	0.4269	1.6230	1.1916	0.9532
21.0	0.9933	0.5584	0.2690	1.3758	0.8739	0.4274	1.6394	1.2055	0.9538
22.0	1.0050	0.5706	0.2689	1.3855	0.8786	0.4279	1.6555	1.2083	0.9543
23.0	1.0243	0.5750	0.2688	1.4030	0.8830	0.4284	1.6804	1.2220	0.9549
24.0	1.0348	0.5792	0.2687	1.4116	0.8871	0.4288	1.6960	1.2466	0.9554
25.0	1.0447	0.5909	0.2693	1.4283	0.8994	0.4292	1.7115	1.2601	0.9558
26.0	1.0628	0.5948	0.2693	1.4360	0.9031	0.4296	1.7176	1.2736	0.9563
27.0	1.0719	0.5985	0.2693	1.4521	0.9065	0.4299	1.7330	1.2870	0.9567
28.0	1.0892	0.6020	0.2694	1.4590	0.9098	0.4342	1.7482	1.3003	0.9678
29.0	1.0976	0.6133	0.2695	1.4745	0.9129	0.4346	1.7633	1.3136	0.9683
30.0	1.1055	0.6165	0.2695	1.4809	0.9246	0.4349	1.7782	1.3269	0.9687

Table 7.2: A/L measure for curve reconstruction of the curved-inclined image for various λ

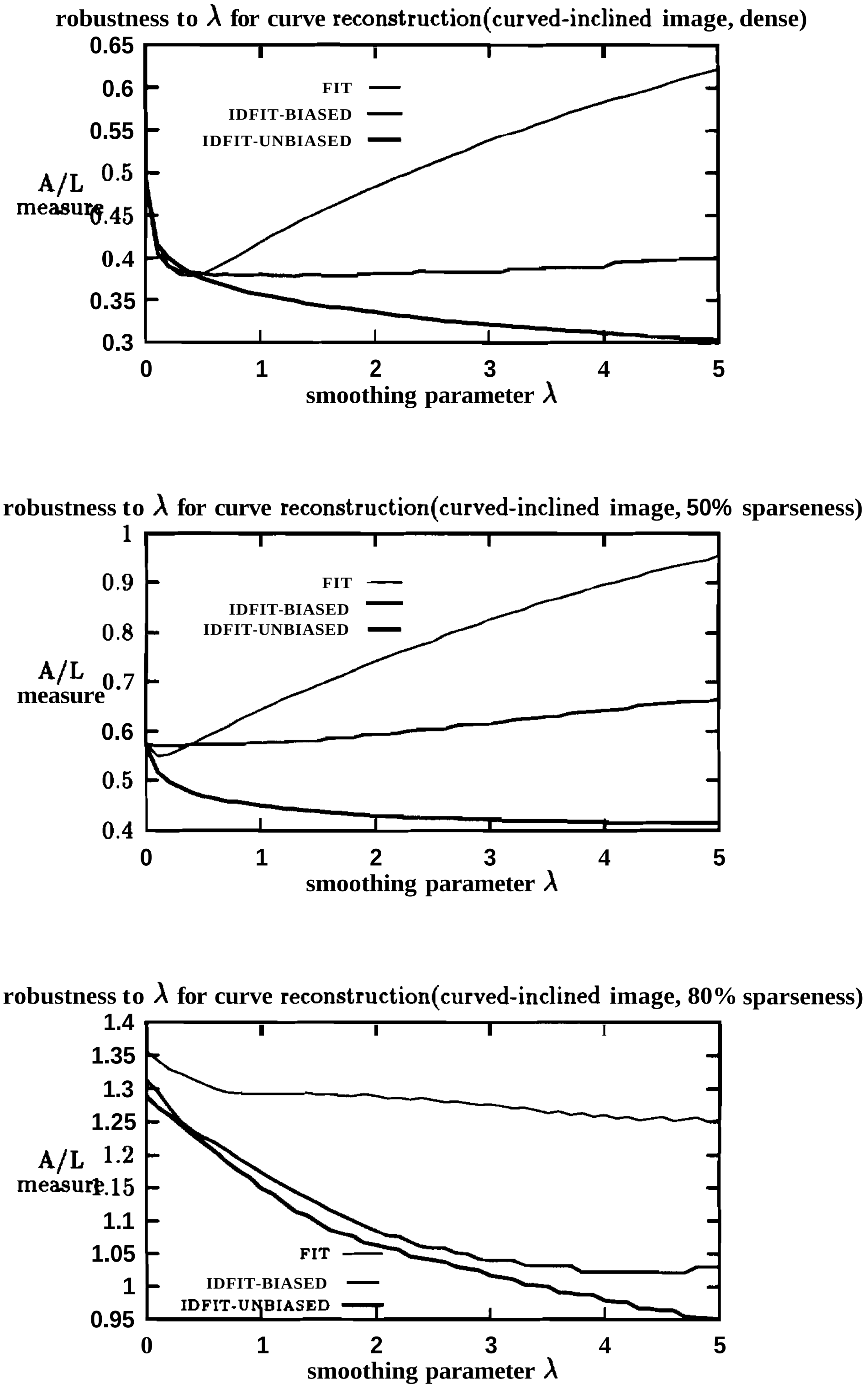

Figure 7.25: Robustness of curve reconstruction to X

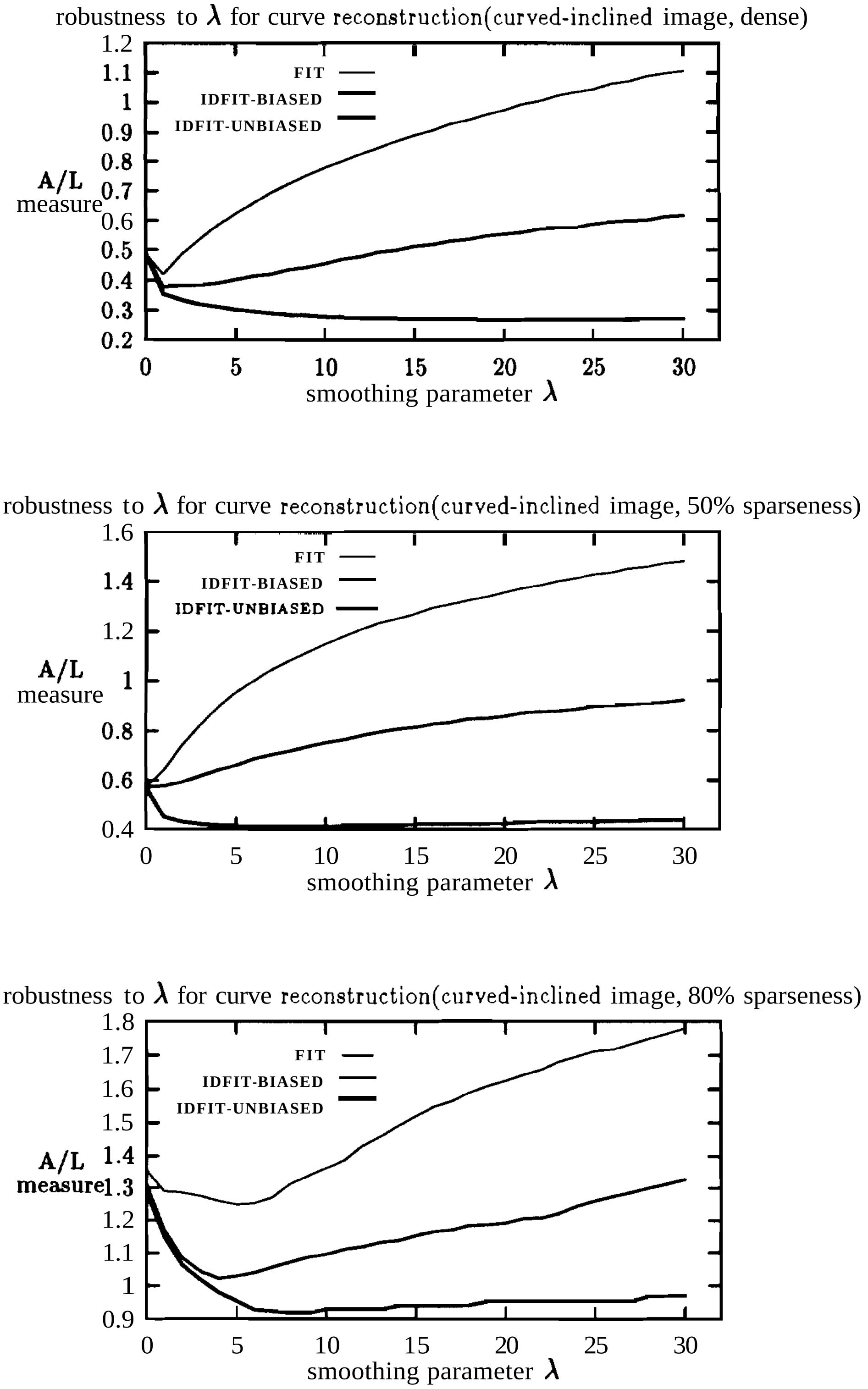

robustness to λ for curve reconstruction(curved-inclined image, dense)

robustness to λ for curve reconstruction(curved-inclined image, 50% sparseness)

robustness to λ for curve reconstruction(curved-inclined image, 80% sparseness)

Figure 7.26: Robustness of curve reconstruction to X

Chapter 8

Conclusion

In contrast to previous work, the first order energy functionals with unbiased derivative estimates presented here for curve reconstruction and surface reconstruction are the first to achieve both preservation of discontinuities and approximate invariance. They also have the important property of robustness to the smoothing parameter λ. These properties enable the proposed methods for reconstruction of curves and surfaces to perform much better than other existing methods on dense noisy data and work especially well on sparse noisy range data. Curved surfaces (or curved sections in the case of curve reconstruction) are well reconstructed although a first order model is employed. In addition, the new first order reconstruction methods for curve reconstruction and surface reconstruction can be used for dense data simply as a noise filter without causing the problem of loss of resolution.

Acknowledgement

The authors gratefully acknowledge Michigan State University's Pattern Recognition and Image Processing Laboratory for the range images “jumble2**” and “**foot2**” used in this work.**

Bibliography

[1] J. Aloimonos and D. Schulman. Learning early-vision computations. *J.* Optical Society of America, 6(6), June 1989.

[2] A. Blake. Reconstructing a visible surface. In Proc. AAAI Conference, pages 23–26, 1984.

[3] A. Blake and A. Zisserman. Invariant surface reconstruction using weak continuity constraints. In Proc. IEEE Int. Conf. Computer Vision and Pattern Recognition, pages 22–26, Miami, FL, June 1986.

[4] A. Blake and A. Zisserman. Visual Reconstructions. MIT Press, Cambridge, MA, 1987.

[5] T. E. Boult and J. R. Kender. Visual surface reconstruction using sparse depth data. In Proc. IEEE Int. Conf. Computer Vision and Pattern Recognition, pages 68–76, Miami, FL, June 1986.

[6] D. M. Chelberg and J. Yi. Range image segmentation using regularization. In Proceedings of the SPIE International Conference on Intelligent Robot and Advanced Systems, pages 336–347, Boston, MA, November 1991.

[7] P. B. Chou and C. M. Brown. Multimodal reconstruction and segmentation with Markov random fields and HCF optimization. In Proc. DARPA Image Understanding Workshop, 1988.

[8] C. Chu and Alan C. Bovik. Visible surface reconstruction via local Minimax approximation. Pattern Recognition, 21.(4):303–312, 1988.

[9] D. Geiger and F. Federico. Parallel and deterministic algorithms from MRF's: Surface reconstruction. IEEE Trans. *Patt.* Anal. Machine *Intell.*, 13(5):401–412, May 1991.

[10] S. Geman and D. Geman. Stochastic relaxation, Gibbs distributions, and the Bayesian restoration of images. IEEE Trans. *Patt.* Anal. Machine *Intell.*, 6(6), November 1984.

[11] W. E. Grimson and T. Pavlidis. Discontinuity detection for surface reconstruction. Computer Vision, Graphics, and Image Processing, 30:316–330, 1985.

[12] P. J. Huber. Robust Statistics. John Wiley & Sons, New York, 1981.

[13] K. Ikeuchi and T. Kanade. Modeling sensors and applying sensor model to automatic generation of object recognition program. In Proc. DARPA Image Understunding Workshop, pages 697–710, 1987.

[14] V. E. Johnson, W. H. Wong, X. Hu, and C. Chen. Image restoration using Gibbs priors: Boundary modeling, treatment of blurring, and selection of hyperparameter. IEEE Trans. Patt. Anal. Machine *Intell.*, 13(5):413–425, May 1991.

[15] S. Kirkpatrick, C. D. Gelatt Jr., and M. P. Vecci. Optimization by simulated annealing. Science, 220:671–680, 1983.

[16] D. Lee and T. Pavlidis. One-dimensional regularization with discontinuities. IEEE Trans. Patt. Anal. Machine *Intell.*, 10(6), July 1988.

[17] S. Z. Li. Invariant surface segmentation through energy minimization with discontinuities. Int. J. Comput. Vision, 5(2):161–194, 1990.

[18] J. Marroquin, S. Mitter, and T. Poggio. Probablistic solution of ill-posed problems in computational vision. J. American Statistical Association, 82(397):76–89, March 1987.

[19] D. Mumford and J. Shah. Boundary detection by minimizing functionals. In Proc. IEEE Int. Conf. Computer Vision and Pattern Recognition, San Francisco, CA, 1985.

[20] P. Perona and J. Malik. Scale-space edge detection using anisotropic diffusion. IEEE Trans. Patt. Anal. Machine *Intell.*, 12(7):629–639, July 1990.

[21] W. H. Press, B. P. Flannery, S. A. Teukolsky, and W. T. Vetterling. Numerical Recipes in C: The Art of Scientific Computing. Cambridge University Press, Cambridge, 1988.

[22] S. S. Sinha and B. G. Schunck. A two stage algorithm for discontinuity-preserving surface reconstruction. IEEE Trans. Patt. Anal. Machine *Intell.*, 14(1):36–55, November 1988.

[23] S. S. Sinha and B. G. Schunck. Discontinuity preserving surface reconstruction. In Proc. IEEE Int. Conf. Computer Vision and Pattern Recognition, pages 229–234, San Diego, CA, June 1989.

[24] R. L. Stevenson and E. J. Delp. Fitting curves with discontinuities. In Proc. Int. Workshop on Robust Computer Vision, Seattle, WA, 1990.

[25] R. L. Stevenson and E. J. Delp. Invariant recovery of curves in m-dimensional space from sparse data. J. Optical Society of America, 7(3), March 1990.

[26] R. L. Stevenson and E. J. Delp. Surface reconstruction with discontinuities. In Proceedings of the SPIE International Conference on Computer Vision and Graphics 11, Boston, MA, November 1991.

[27] R. L. Stevenson and E. J. Delp. Viewpoint invariant recovery of visual surfaces from sparse data. IEEE Trans. Patt. Anal. Machine *Intell.*, 14(9):897–909, September 1992.

[28] R. Szeliski. Bayesian modeling of uncertainty in low-level vision. Int. J. Comput. Vision, 5(3):271–301, 1990.

[29] R. Szeliski. Fast surface interpolation using hierarchical basis functions. IEEE Trans. Patt. Anal. Machine *Intell.*, 12(6):513–520, June 1990.

[30] D. Terzopoulos. Multilevel resolution of visual surfaces: Variational principles and finite element representations. In A. Rosenfeld, editor, Multiresolution Image Processing and Analysis, pages 237–310. Springer-Verlag, New York, 1984.

[31] D. Terzopoulos. Regularization of inverse visual problems involving discontinuities. IEEE Trans. Patt. Anal. Machine *Intell.*, 8(4):413–423, July 1986.

[32] D. Terzopoulos. The computation of visible-surface representations. IEEE Trans. Patt. Anal. Machine *Intell.*, 10(4):417–438, July 1988.

[33] A. M. Thompson, J. C. Brown, K. W. Kay, and D. M. Titterington. A study of methods of choosing the smoothing parameter in image restoration by regularization. IEEE Trans. Patt. Anal. Machine *Intell.*, 13(4), April 1991.

[34] J. Yi and D. M. Chelberg. Discontinuity-preserving and viewpoint invariant reconstruction of visible surfaces from sparse data using a first order regularization. In Proceedings of the IEEE International Conference on Automation, robotics, and Computer Vision, volume 1, pages cv5.1.l–cv5.1.5, Singapore, September 1992.

[35] J. Yi and D. M. Chelberg. Computation of the volume and the surface area: With an application to an invariant measure for surface reconstruction results. submitted to CVGIP: Graphical Models and Image Processing, 1993.